Nonthermal plasma density redistribution in planetary magnetospheres due to ion-cyclotron waves

Joaquín Espinoza-Troni[1], Felipe A Asenjo[2], and Pablo S Moya[1]

[1] Departamento de Física, Facultad de Ciencias, Universidad de Chile, Santiago, Chile
e-mail: joaquinun@gmail.com, pablo.moya@uchile.cl

[2] Facultad de Ingeniería y Ciencias, Universidad Adolfo Ibáñez, Santiago, Chile.
e-mail: felipe.asenjo@uai.cl

ABSTRACT

Context. Planetary magnetospheres throughout the Solar System exhibit diverse plasma environments in which ultra-low-frequency pulsations can induce nonlinear ponderomotive effects. Recent analytical studies have predicted a significant effect of the Kappa velocity distribution on the ponderomotive force (PF) induced by electromagnetic ion cyclotron (EMIC) waves. Since suprathermal populations modeled by Kappa distributions are ubiquitous in planetary magnetospheres (from Mercury to the ice giants), their effect on ponderomotive phenomena must be accounted for.

Aims. We investigated the field-aligned plasma density redistribution driven by the PF of traveling EMIC waves by performing a comparative analysis in the different regimes that are characteristic of the planetary magnetospheres of our Solar System.

Methods. We applied a generalized slow-timescale force balance equation to model the stationary plasma density solutions for each planetary magnetosphere. The model incorporates the PF induced by traveling EMIC waves in low-beta plasmas ($\beta \ll 1$) with isotropic Kappa distributions. To enable a systematic comparison, the wave modulation is described using the Wentzel–Kramers–Brillouin approximation in a dipole magnetic field model, neglecting curvature effects to first order in planetary fields.

Results. We find that the plasma response varies significantly depending on the magnetospheric parameters: a decrease in the kappa parameter and an increase in plasma beta counteract plasma accumulation towards the equator. In low-beta planetary environments, nonthermal effects significantly reduce the nonlinear response to short-period pulsations without altering the qualitative behavior predicted by Maxwellian models. We also characterized the variation in the critical parameter governing the phase transition between equatorial density minima and maxima with the specific combinations of plasma beta, the kappa parameter, and L-shell observed in the Solar System. Furthermore, applying this model to the dayside low-beta inner magnetospheres of Earth, Jupiter, and Saturn revealed that the PF exerts a substantial effect primarily during exceptionally high-amplitude EMIC wave events.

Conclusions. Our analytical study demonstrates that the nonthermal properties of plasma are a governing factor in the field-aligned density redistribution driven by ultra-low-frequency waves. These results highlight the necessity of incorporating nonthermal effects to accurately model ponderomotive phenomena in the multifaceted types of planetary magnetospheres of the Solar System.

Key words. Plasma density redistribution – Ultra-low frequency waves – Ponderomotive force – Planetary magnetospheres

1. Introduction

Planetary magnetospheres act as cavities supporting diverse ultra-low-frequency (ULF) waves. While most studies focus on the Earth's magnetosphere, ULF waves have been observed extensively in the magnetospheres of other planets. The Mercury magnetosphere exhibits ULF waves in the ion cyclotron frequency range, as observed by the Mariner 10 (Russell 1989; Kim et al. 2015) and MErcury Surface, Space ENvironment, GEochemistry, and Rangin (MESSENGER) (Boardsen et al. 2009b,a, 2012) spacecraft missions. Farther out, EMIC-mode ULF waves were detected at Jupiter by the Ulysses spacecraft (Petkaki & Dougherty 2001), and, more recently, a global statistical analysis of Juno data has further characterized Jovian ULF waves (Sun et al. 2024). At Saturn, the Voyager 1 and 2 (Orlowski et al. 1992) and Cassini (Kleindienst et al. 2009; Andrés et al. 2013) spacecraft detected ULF waves, while Voyager 2 observations also revealed ULF activity at the ice giants Uranus and Neptune (Russell & Lepping 1992; Farrell et al. 1993).

Although the underlying physics is shared, planetary magnetospheres differ in size, structure, and composition, affecting ULF propagation. For instance, Jupiter and Saturn exhibit longer-period pulsations than Earth because their magnetospheres are larger. The ULF range can indeed be extended here, passing from 0.2–600 s at Earth to tens of minutes for Jupiter and Saturn (supporting frequencies of $<$ 1 mHz) (Delamere 2016). Historically, these waves have been classified according to terrestrial standards. They correspond to geomagnetic pulsations spanning frequencies from the lowest supported by the Earth's magnetospheric cavity to various ion gyrofrequencies, corresponding to a range from 0.001–5 Hz (Allan & Poulter 1992; Hughes 1994; Hartinger et al. 2022). These are classified into five groups based on their period: Pc1 (0.2–5 s), Pc2 (5–10 s), Pc3 (10–45 s), Pc4 (45–150 s), and Pc5 (150–600 s) (Hughes 1994).

These perturbations can also be broadly classified into long- and short-period pulsations (Kangas et al. 1998). Long-period pulsations span the lower end of the frequency band, with wavelengths comparable to the size of Earth's magnetosphere, and they are often well described using a magnetohydrodynamic (MHD) approximation. In contrast, short-period pulsations (Pc1 and Pc2), typically observed as electromagnetic ion cyclotron

Article published by EDP Sciences, to be cited as https://doi.org/10.1051/0004-6361/202660106

(EMIC) traveling waves, are better described by other mathematical approximations, such as multifluid or kinetic formalisms (Mursula et al. 2001).

Beyond their classification, ULF waves take part in several magnetospheric phenomena. Extensive research has been conducted in the past decades on the effect of ULF pulsations on the background magnetospheric plasma due to the ponderomotive force (PF) (Lundin & Guglielmi 2007; Lundin & Lidgren 2022). This time-averaged nonlinear force arises from the interaction of quasi-monochromatic or spatially inhomogeneous waves with plasma (Kentwell & Jones 1987).

The PF plays an essential role in the physics of ULF waves and significantly contributes to the plasma density redistribution in planetary magnetospheres. It provides a useful framework for studying complex wave-plasma interactions on slow timescales and has frequently been invoked to describe a wide range of phenomena. For instance, this nonlinear effect can partially contribute to plasma acceleration in the polar cusps through the action of traveling Pc1-2 Alfvén and EMIC waves (Guglielmi & Lundin 2001a), generate ambipolar electric fields impacting heavy ion acceleration (Li & Temerin 1993; Guglielmi & Feygin 2023; Guglielmi et al. 2024), and potentially affect solar wind deceleration in the foreshock (Guglielmi et al. 2025). Most theoretical work has focused on Earth, investigating effects from cavity modes to toroidal eigenmodes in simplified dipole models (Allan et al. 1991; Allan 1993, 1994; Guglielmi et al. 1999) or non-dipolar configurations (Antonova & Shabanskii 1968; Nekrasov & Feygin 2012a, 2015, 2016, 2018), and correlating with observational features like density clouds (Chappell 1974; Anderson et al. 1992) or interplanetary magnetic field orientation (Guglielmi & Feygin 2018). However, the universality of these waves suggests that similar processes occur elsewhere in the Solar System.

Understanding the impact of ULF waves in these diverse environments requires considering the specific plasma properties of each planet. Due to low collision rates, most space plasmas deviate from thermal equilibrium and are well described by the family of Kappa distributions (Lazar et al. 2023). These distributions depend on the spectral index κ, allowing the modeling of suprathermal tails widely observed in near-Earth space environments (Lazar & Fichtner 2021). Such suprathermal tails are ubiquitous in the Solar System; they have been observed and modeled with power-law or Kappa distributions in the magnetosphere of Jupiter (Mauk et al. 1996, 2004), Saturn (Krimigis et al. 1983; Dialynas et al. 2009), Mercury (Christon 1987), Uranus (Krimigis et al. 1986; Mauk et al. 1987), and Neptune (Krimigis et al. 1989; Mauk et al. 1991), with kappa values that can vary between 3–10 depending on the magnetospheric zone and the planet (Kirpichev & Antonova 2020). Recent analytical studies have highlighted the effect of these nonthermal effects on the PF. Espinoza-Troni et al. (2023) showed that in low-temperature unmagnetized plasmas with isotropic Kappa distributions, the κ parameter significantly affects the temporal term of the PF due to transverse waves. Espinoza-Troni, Joaquín et al. (2024) extended these results to low-temperature magnetized plasmas, finding that for all terms of the PF, the impact of the Kappa distribution cannot always be neglected and that it increases with the plasma beta.

We extend previous studies of the plasma density redistribution driven by the PF of traveling EMIC waves in nonthermal plasmas by expanding the context to analyze and compare different planetary magnetospheres. We employ the PF expressions from Espinoza-Troni, Joaquín et al. (2024), which assumed a field-aligned propagation of EMIC waves in low-temperature isotropic Kappa plasmas. A dipole approximation of planetary magnetospheres was adopted, enabling a first comparative assessment across the Solar System. Although rough for non-dipolar configurations such as Neptune and Uranus (Holme & Bloxham 1996), this approach provides a useful first-order assessment of nonthermal effects on plasma redistribution driven by the PF in the Solar System.

This paper is structured as follows: Section 2 reviews the slow-timescale fluid equations of the plasma and introduces the notation and normalization we use throughout. Section 3 provides a brief overview of the PF and its different terms. Section 4 presents the ion-dispersion relation of EMIC waves for isotropic Kappa plasmas in low-beta conditions. Section 5 computes the different PF terms. To this end, the magnitude of the electric wave field is determined as a function of the background variables by solving the wave equation in the Wentzel–Kramers–Brillouin (WKB) approximation. Section 6 presents numerical solutions for the differential equation of the plasma density redistribution and analyzes its behavior for different values of the plasma beta, the L-shell, and the wave frequency in the context of the planetary magnetospheres of our Solar System. Section 7 analyzes the dependence of the magnitude of the ponderomotive effect on the relative wave amplitude and the average magnetospheric conditions typically observed in the planetary magnetospheres in our Solar System. Finally, Section 8 summarizes the main conclusions of this work.

2. Slow-timescale one-fluid equation

In this section, we review the equations governing the slow-timescale dynamics of plasma under the effect of fast-timescale electromagnetic waves in the magnetospheres of generic planets. The slow-timescale component of plasma quantities is defined as the low-pass filtered version of the quantity with respect to the wave carrier frequency. Accordingly, we introduce the time-average operator as

$$\langle A \rangle = \frac{1}{\tau} \int_t^{t+\tau} A dt, \tag{1}$$

where A is a plasma quantity and $\tau \gg 2\pi/\omega$, with ω the carrier frequency of the fluctuations. The plasma variables can then be decomposed into slow- and fast-timescale components,

$$A = \langle A \rangle + \tilde{A}, \tag{2}$$

where $\tilde{A}$ denotes the fast-timescale contribution. We also define the following scale parameters:

$$\frac{|\tilde{A}|}{A_0} \sim \zeta, \qquad \frac{1}{|\langle A \rangle|} \left| \frac{\partial \langle A \rangle}{\partial t} \right| \sim \lambda\omega, \qquad \frac{1}{|\langle A \rangle|} |\nabla \langle A \rangle| \sim \eta k, \tag{3}$$

where $\zeta \ll 1$, $\lambda \ll 1$, and $\eta \ll 1$ are small parameters, A_0 is the characteristic large-scale value of the corresponding variable, and k is the wavenumber of the fluctuations. Within this framework, the fast-timescale terms are treated as first-order perturbations, and the slow-timescale quantities are assumed to vary only weakly in space and time over a wave period. By construction, the fast-timescale fluctuations average to zero, $\left\langle \tilde{A} \right\rangle = 0$.

This timescale separation (Eq. 2) can be applied to the plasma fluid and Maxwell equations and then averaged to obtain the slow-timescale fluid equations of the plasma (Tskhakaya 1981; Karpman & Shagalov 1982; Lee & Parks 1983). The fast-timescale equations are recovered by subtracting the slow-timescale equations from the full system under the approximation $\left\langle \tilde{f}\tilde{g} \right\rangle - \tilde{f}\tilde{g} \simeq 0$, and retaining terms up to second order in $\tilde{A}$.

With these considerations, the slow-timescale momentum equation becomes

$$m_\alpha \langle n_\alpha \rangle \left[\frac{\partial \mathbf{u}_\alpha}{\partial t} + \mathbf{u}_\alpha \cdot \nabla \mathbf{u}_\alpha \right] = q_\alpha \langle n_\alpha \rangle \langle \mathbf{E} \rangle$$
$$+ \frac{q_\alpha \langle n_\alpha \rangle}{c} \mathbf{u}_\alpha \times \langle \mathbf{B} \rangle - \nabla \cdot \langle \mathbf{P}_\alpha \rangle + m_\alpha \langle n_\alpha \rangle \mathbf{g} + \mathbf{f}_\alpha, \tag{4}$$

where the subscript α denotes the species, n_α is the number density, $\mathbf{B}$ is the magnetic field, $\mathbf{E}$ is the electric field, $\mathbf{g}$ is the gravity acceleration of the planet (nonconstant), and $\mathbf{u}_\alpha$ is the renormalized slow-timescale fluid velocity, redefined for consistency with the continuity equation. Different renormalizations provide different interpretations of $\mathbf{u}_\alpha$ as discussed in Kentwell & Jones (1987). Still, since we consider stationary electromagnetic field wave amplitudes and the PF along the geomagnetic field (see below), this choice does not affect our results (see Eqs. (30) and (34) of Karpman & Shagalov (1982)). The PF $\mathbf{f}_\alpha$ encompasses the correlation effects of the fast-timescale quantities due to the electromagnetic field perturbation in the slow-timescale dynamics. In the next section, we review its expression within the Washimi-Karpman formalism.

We considered a quasi-neutral plasma composed of electrons and ions with isotropic pressure tensors. Assuming force balance along the background magnetic field lines, we obtained

$$0 = -\nabla_\parallel p + M n g_\parallel + f_\parallel, \tag{5}$$

where $\nabla_\parallel = \hat{\mathbf{b}} \cdot \nabla$, $g_\parallel = \hat{\mathbf{b}} \cdot \mathbf{g}$, $f_\parallel = \hat{\mathbf{b}} \cdot (\mathbf{f}_e + \mathbf{f}_i)$, $M = m_i + m_e \approx m_i$, $n = \langle n_e \rangle = \langle n_i \rangle$ and $\hat{\mathbf{b}} = \langle \mathbf{B} \rangle / |\langle \mathbf{B} \rangle|$. We took the electron and ion temperatures to be equal $T = T_i = T_e$, with T the temperature in the Maxwellian limit. For the pressure closure, we adopted (Lazar, M. et al. 2017)

$$p = \left(\frac{\kappa}{\kappa - 3/2} \right) 2 k_B T n = \left(\frac{\kappa}{\kappa - 3/2} \right) (\beta_0 c_{A0}^2 M n_0) \bar{n}, \tag{6}$$

where k_B is the Boltzmann constant, $n_0 = n(x_\parallel = 0)$ is the equatorial number density at the equator (i.e., at $x_\parallel = 0$), with $x_\parallel$ the distance along the geomagnetic field lines, $\bar{n} = n/n_0$ is the normalized number density, $\beta_{\kappa 0} = [\kappa - (\kappa - 3/2)]\beta_0$ with $\beta_0 = 8\pi n_0 k_B T / B_0^2$ the plasma beta at the equator, and $B_0 = |\langle \mathbf{B}(x_\parallel = 0) \rangle|$ the magnitude of the background equatorial magnetic field. The kappa parameter κ quantifies deviations from the thermal equilibrium. When we normalize the directional derivative with the planet radius R_p, that is, $\bar{\nabla}_\parallel = R_p \nabla_\parallel$, the force balance equation becomes

$$0 = -\beta_{\kappa 0} \bar{\nabla}_\parallel \bar{n} + C_g \bar{n} \bar{g}_\parallel + \nu^2 \bar{f}_\parallel, \tag{7}$$

where the PF is normalized as $\bar{f}_\parallel = 4\pi R_p f_\parallel / (B_0^2 \nu^2)$, with ν as the ratio of the wave amplitude and the background equatorial magnetic field (to be defined more precisely below). The gravity acceleration was normalized as $\bar{g}_\parallel = g_\parallel / g_0$ with $g_0 = G M_p / R_p^2$ the gravity of the planet on its surface, with G the universal gravity constant, and M_p the mass of the planet. We also defined the dimensionless parameter $C_g = (g_0 R_p / c^2)(c/c_{A0})^2$, which accounts for gravitational effects, with c the speed of light, and $c_{A0} = B_0 / \sqrt{4\pi M n_0}$ the equatorial Alfvén velocity.

To calculate the PF, we also required an expression for the field-aligned spatial variation of the fast-timescale electromagnetic field. From the Maxwell equations, the wave equation for the fast-timescale electric field is

$$4\pi \frac{\partial \tilde{\mathbf{J}}}{\partial t} = c^2 \nabla^2 \tilde{\mathbf{E}} - c^2 \nabla (\nabla \cdot \tilde{\mathbf{E}}) - \frac{\partial^2 \tilde{\mathbf{E}}}{\partial t^2}, \tag{8}$$

where $\tilde{\mathbf{J}}$ and $\tilde{\mathbf{E}}$ are the fast-timescale current density and electric field, respectively (Lee & Parks 1998).

3. Washimi-Karpman ponderomotive force

The PF is a nonlinear phenomenon arising from the interaction of a high-frequency field (relative to the slow background) with the plasma, affecting its slow-timescale dynamics (Kentwell & Jones 1987). In what follows, we adopt the Washimi-Karpman PF formalism (Washimi & Karpman 1976; Karpman & Shagalov 1982).

In this framework, the fast-timescale electromagnetic field is represented as a quasi-monochromatic wave $\tilde{\mathbf{E}} = (1/2) \left[\hat{\mathbf{E}}(\mathbf{r}, t) e^{-i\omega t} + \hat{\mathbf{E}}^*(\mathbf{r}, t) e^{i\omega t} \right]$, where $|\hat{\mathbf{E}}(\mathbf{r}, t)|$ varies slowly in space and time compared to the wave-carrier frequency and wavenumber. In the presence of a background magnetic field, the Washimi-Karpman PF $\mathbf{f} = \sum_\alpha \mathbf{f}_\alpha$ consists of four contributions. A term $\mathbf{f}_{(s)}$ associated with the spatial modulation of the electric field magnitude, a term $\mathbf{f}_{(t)}$ associated with the temporal modulation of the electric field magnitude, another term $\mathbf{f}_{(m)}$ associated with the nonlinear magnetically induced moment, and another term $\mathbf{f}_{MMP}$ associated with the spatial variation in the background magnetic field (Espinoza-Troni et al. 2023; Espinoza-Troni, Joaquín et al. 2024), thus

$$\mathbf{f} = \mathbf{f}_{(s)} + \mathbf{f}_{(t)} + \mathbf{f}_{(m)} + \mathbf{f}_{MMP}. \tag{9}$$

We neglected the PF temporal term of $\mathbf{f}_{(t)}$, since the wave amplitude is regarded as stationary. This approximation was considered for simplicity and is valid when the wave amplitude temporal modulation is assumed to be much slower than the transit time of the wave packet over a characteristic length of the field (as also done by Guglielmi et al. (1999); Nekrasov & Feygin (2012b)). We also omitted $\mathbf{f}_{(m)}$ since this term acts perpendicular to the background magnetic field and does not contribute to the force balance equation along the geomagnetic field lines. The spatial term is given by

$$\mathbf{f}_{(s)} = \frac{1}{16\pi} (\varepsilon_{ij} - \delta_{ij}) \nabla \hat{E}_i^* \hat{E}_j, \tag{10}$$

where ε_{ij} are the components of the dielectric tensor, and δ_{ij} is the Kronecker delta (Washimi & Karpman 1976). This contribution is well known in nonlinear laser-plasma interactions, where it can induce density modifications (Hora 1969). Modification of the local dielectric tensor also affects the wave propagation in plasmas. The remaining contribution $\mathbf{f}_{MMP}$ originates from the interaction between the background magnetic field gradient and the nonlinear magnetic moment induced in the particles by the wave. This term is usually called magnetic moment pumping (MMP) (Lundin & Guglielmi 2007), and is given by

$$\mathbf{f}_{(MMP)} = \mathcal{M} \nabla |\langle \mathbf{B} \rangle|, \tag{11}$$

where $\mathcal{M} = (1/16\pi)(\partial \varepsilon_{ij} / \partial |\langle \mathbf{B} \rangle|) E_i^* E_j$ is the magnetic moment induced by the wave. For EMIC waves, this term points toward regions of decreasing magnetic field strength (Espinoza-Troni, Joaquín et al. 2024). For this reason, it has been proposed as part of a mechanism that accelerates ions in the polar regions, thereby contributing to the polar wind (Lundin & Hultqvist 1989; Guglielmi & Lundin 2001b; Guglielmi et al. 2004). It can also lead to plasma accumulation in the minimum of the geomagnetic field, which is the equator for a dipolar magnetosphere, as discussed in Guglielmi et al. (1995, 1999); Nekrasov & Feygin (2016), and analyzed below.

4. Ion-cyclotron dispersion relation for kappa-distributed plasmas

In this investigation, we considered EMIC waves propagating along the geomagnetic field lines of different planets in a plasma characterized by an isotropic Kappa distribution,

$$\mathcal{F}_{\kappa\alpha}(\mathbf{v}) = \frac{\langle n_s \rangle}{\pi^{3/2} v_{th\alpha}^3 \kappa^{3/2}} \frac{\Gamma(\kappa+1)}{\Gamma(\kappa-1/2)} \left(1 + \frac{v^2}{\kappa v_{th\alpha}^2}\right)^{-(\kappa+1)}. \tag{12}$$

Here, $\mathcal{F}_{\kappa\alpha}$ is the Kappa distribution for the species α, $v_{th\alpha}\{= \sqrt{2k_B T_\alpha/m_\alpha}\}$ is their thermal velocity, T_α is their temperature, and Γ is the Gamma function. This is the simplest form of the family of Kappa distributions, with the Maxwellian distribution recovered in the limit $\kappa \to \infty$, and it is valid for $\kappa > 3/2$. Planetary magnetospheres are often well modeled by combinations or modifications of Kappa distributions (Lazar & Fichtner 2021). Although real distributions can exhibit temperature anisotropies and depend strongly on the specific region and space-weather conditions, we adopted this isotropic form as a first step to assess the effects of suprathermal populations found in planetary magnetospheres on ponderomotive interactions.

Espinoza-Troni, Joaquín et al. (2024) derived the dielectric tensor for Kappa distributed plasmas under the low-temperature approximation $kv_{th\alpha}/(\omega \pm |\Omega_\alpha|) \ll 1$, where $\Omega_\alpha = q_\alpha |\langle \mathbf{B} \rangle| / m_\alpha c$ is the gyrofrequency of the species α. For a left-handed polarized wave, with the carrier wave frequency lower than the ion gyrofrequency in a proton-electron plasma, the dielectric eigenvalue of EMIC waves with field-aligned propagation is approximated as

$$\varepsilon(\omega, k) \approx \varepsilon_c(\omega) - \frac{k^2 c^2}{\omega^2} \delta_\kappa(\omega), \tag{13}$$

where $\varepsilon_c(\omega)$ is the EMIC dielectric eigenvalue for cold plasmas

$$\varepsilon_c(\omega) = 1 + \left(\frac{c}{c_A}\right)^2 \frac{\Omega_i}{(\Omega_i - \omega)}, \tag{14}$$

and $\delta_\kappa(\omega)$ is the finite-temperature correction with the nonthermal effects

$$\delta_\kappa(\omega) = -\left(\frac{\kappa}{\kappa - 3/2}\right) \frac{\beta}{2} \frac{\omega \Omega_i^2}{(\Omega_i - \omega)^3}, \tag{15}$$

with $\beta = 8\pi n k_B T / |\langle \mathbf{B} \rangle|^2$ the plasma beta. On the other hand, the dispersion relation is given by

$$\varepsilon(\omega, k) = \frac{k^2 c^2}{\omega^2}. \tag{16}$$

Using this expression, we can include the dispersion relation in Equation (13), and since our approximation is consistent for low-beta regimes, we can consider up to the second order of $\delta_\kappa(\omega)$. Then, we have that

$$\varepsilon(\omega, k(\omega)) = \frac{\varepsilon_c}{(1 + \delta_\kappa)} \approx \varepsilon_c (1 - \delta_\kappa). \tag{17}$$

We also introduced the following normalization. We denote $\mathcal{B} = |\langle \mathbf{B} \rangle| / B_0$ as the normalized background magnetic field, $\Omega_{i0} = qB_0/mc$ the ion gyrofrequency at the equator, and $\bar{\omega} = \omega/\Omega_{i0} < 1$ the normalized frequency with respect to the equator gyrofrequency. Therefore, from Equations (14) and (15), we have that

$$\varepsilon_c(\omega) \approx \left(\frac{c}{c_{A0}}\right)^2 \frac{\bar{n}}{\mathcal{B}(\mathcal{B} - \bar{\omega})} = \left(\frac{c}{c_{A0}}\right)^2 K\bar{n}, \tag{18}$$

$$\delta_\kappa(\omega) = -\frac{\beta_{\kappa 0}}{2} \frac{\bar{\omega}\bar{n}}{(\mathcal{B} - \bar{\omega})^3} = \beta_{0\kappa} P \bar{n}, \tag{19}$$

where we considered that $c/c_{A0} \gg 1$, and we defined $K = 1/[\mathcal{B}(\mathcal{B} - \bar{\omega})]$ and $P = -(1/2)\bar{\omega}/(\mathcal{B} - \bar{\omega})^3$. These expressions are valid away from the resonance region $\mathcal{B} \approx \bar{\omega}$, where the approximation breaks down; our PF expression implicitly assumes an adiabatic approximation, which is violated near gyro-resonance (Lamb et al. 1984; Kono & Sanuki 1987).

5. Ponderomotive force for ion-cyclotron waves

In this section, we calculate the various PF terms for EMIC waves in a low-beta nonthermal plasma. Espinoza-Troni, Joaquín et al. (2024) computed the coefficients accompanying the spatial and temporal modulation of the wave in the PF for an isotropic Kappa plasma. Nevertheless, to obtain the full expression for the PF and complete the set of equations, we need the magnitude of the electric wave field $\hat{\mathbf{E}}(\mathbf{r})$ as a function of the background variables. To obtain this expression, we assumed that $\hat{\mathbf{E}}(\mathbf{r})$ has a left-handed polarization,

$$\hat{\mathbf{E}}(\mathbf{r}) = \hat{E}(x_\parallel)\,(\hat{\mathbf{x}}_{\perp 1} - i\hat{\mathbf{x}}_{\perp 2}), \tag{20}$$

where $\hat{\mathbf{x}}_{\perp 1}$ and $\hat{\mathbf{x}}_{\perp 2}$ are orthogonal coordinates aligned perpendicular to the magnetic field, with $x_\parallel$ the distance along the magnetic field lines. We also considered that $\hat{\mathbf{J}} = \frac{\omega}{4\pi i} [\varepsilon(\omega, k) - 1] \hat{\mathbf{E}}$. To obtain this last relation, the spatial and temporal variations in the slow-timescale quantities must be neglected when Fourier-transforming the first-order perturbations within the kinetic framework of the Vlasov equation (Krall & Trivelpiece 1986). Including these variations would require a more sophisticated analysis, analogous to the approach of Lee & Parks (1998), in which the wave modulation is governed by a generalization of the derivative nonlinear Schrödinger equation. However, in our case, such a procedure would need to be extended using a full kinetic formalism, which is beyond the scope of this work. Therefore, using Equation (8) and neglecting the curvature of the geomagnetic field lines, we obtained

$$\frac{\partial^2 \hat{E}}{\partial x_\parallel^2} + k^2(x_\parallel)\hat{E} = 0. \tag{21}$$

As in other studies of plasma density redistribution by the PF, we neglected the curvature of the geomagnetic field for simplicity (Nekrasov & Feygin 2012b). This is valid when the curvature of the geomagnetic field lines varies very slowly compared to the wave modulation, and it is useful as a first-order approach for studying finite-temperature and nonthermal effects of the PF on the magnetospheric density redistribution of some planets due to traveling waves. In this case, ε (and therefore k^2) depends on slow-timescale variables, which are expected to vary slowly in a wavelength for the Washimi-Karpman formalism to be valid. Therefore, we assumed that $(1/k)(d\varepsilon/dx_\parallel) \ll \varepsilon$, which is the condition for the WKB approximation (Ghatak et al. 1991). Then, using this approximation, we can show that

$$|\hat{E}(x_\parallel)| \propto \frac{1}{k^{1/2}(x_\parallel)} \propto \frac{1}{\varepsilon^{1/4}(x_\parallel)}. \tag{22}$$

Moreover, the magnetic field wave amplitude $|\hat{B}|$ is related to the electric field wave amplitude by

$$|\hat{E}| = \frac{|\hat{B}|}{\varepsilon^{1/2}}. \tag{23}$$

Therefore, we can express $|\hat{E}|^2$ as

$$|\hat{E}|^2 = \left(\frac{B_0^2 \nu^2}{\varepsilon^{1/2}(x_\parallel = 0)}\right)\frac{\alpha}{\varepsilon^{1/2}}, \tag{24}$$

where $\nu = |\hat{B}(x_\parallel = 0)|/B_0 \sim \zeta$ is the ratio of the magnetic field wave amplitude to the background equatorial magnetic field. In our approach, we set $\alpha = 1$ (as in (Nekrasov & Feygin 2012b)), but we retained the explicit term α because Lundin & Guglielmi (2007) derived $\alpha = \mathcal{B}$ by assuming a vanishing divergence for the slow-timescale Poynting flux. Notably, the two approaches yield qualitatively consistent results (not shown). Since the PF is a second-order effect, this parameter is expected to be small. Neglecting the terms on the order of δ_κ^2 since we are in a low-beta plasma regime, we approximated $\varepsilon^{-1/2} \approx \varepsilon_c^{-1/2}(1 + \delta_\kappa/2)$, then

$$|\hat{E}|^2 \approx B_0^2\nu^2\left(\frac{c}{c_{A0}}\right)^{-1}\frac{(1-\bar{\omega})^{1/2}}{\varepsilon_c^{1/2}}\left[\left(1+\frac{\delta_{\kappa 0}}{2}\right)+\frac{\delta_\kappa}{2}\right]\alpha, \tag{25}$$

where $\delta_{\kappa 0} = \delta_\kappa(x_\parallel = 0) = -(1/2)\beta_{\kappa 0}\bar{\omega}/(1-\bar{\omega})^3$.

5.1. Spatial term

The fast-timescale electric field that we considered is an eigenvector of the dielectric tensor ε_{ij}. The spatial term of the PF is then given by (Espinoza-Troni, Joaquín et al. 2024)

$$f_{(s)\parallel} = \frac{1}{16\pi}(\varepsilon - 1)\nabla_\parallel|\hat{E}|^2. \tag{26}$$

Using equations (25) and (17) and neglecting δ_κ^2, we have that

$$\begin{aligned}\bar{f}_{(s)\parallel} &= (A_1 + \beta_{\kappa 0}A_2)\,\bar{n}^{1/2} + \beta_{\kappa 0}A_3\bar{n}^{3/2}\\ &\quad + (A_4 + \beta_{\kappa 0}A_5)\,\bar{n}^{-1/2}\bar{\nabla}_\parallel\bar{n} + \beta_{\kappa 0}A_6\bar{n}^{1/2}\bar{\nabla}_\parallel\bar{n},\end{aligned} \tag{27}$$

where the functions $A_i(x_\parallel)$ (for $i = 1, ..., 6$) are defined in Appendix A with more details of the calculation. The functions $A_i(x_\parallel)$ depend on the the normalized background magnetic field magnitude $\mathcal{B}(x_\parallel)$ and the normalized frequency $\bar{\omega}$.

5.2. Magnetic moment pumping

The MMP term of the PF is given by (Espinoza-Troni, Joaquín et al. 2024)

$$f_{(MMP)\parallel} = \frac{|\hat{E}|^2}{16\pi}\frac{\partial\varepsilon}{\partial\mathcal{B}}\bar{\nabla}_\parallel\mathcal{B}, \tag{28}$$

and then, by replacing the expression for the wave modulation (25) and the finite-temperature dielectric tensor eigenvalue (17), we have that

$$f_{(MMP)\parallel} = (A_7 + \beta_{\kappa 0}A_8)\,\bar{n}^{1/2} + \beta_{\kappa 0}A_9\bar{n}^{3/2}, \tag{29}$$

where functions $A_7(x_\parallel)$, $A_8(x_\parallel)$, and $A_9(x_\parallel)$ are defined in Appendix A and also depend on the normalized background magnetic field magnitude $\mathcal{B}(x_\parallel)$ and the normalized frequency $\bar{\omega}$.

5.3. Total ponderomotive force

Summing expressions (27) and (29) for the spatial and MMP PF terms, respectively, we obtained that the total PF along the geomagnetic field lines $f_\parallel = f_{(s)\parallel} + f_{(MMP)\parallel}$ is given by

$$\begin{aligned}f_\parallel &= [(A_1 + A_7) + \beta_{\kappa 0}(A_2 + A_8)]\,\bar{n}^{1/2} + \beta_{\kappa 0}\,(A_3 + A_9)\,\bar{n}^{3/2}\\ &\quad + (A_4 + \beta_{\kappa 0}A_5)\,\bar{n}^{-1/2}\bar{\nabla}_\parallel\bar{n} + \beta_{\kappa 0}A_6\bar{n}^{1/2}\bar{\nabla}_\parallel\bar{n}.\end{aligned} \tag{30}$$

6. Plasma density redistribution for nonthermal plasmas

6.1. Differential equation for the density redistribution

In this section, we derive and analyze the differential equation governing the redistribution of the plasma density along geomagnetic field lines in the magnetospheres of some planets. We then discuss some analytical properties of this equation.

Using the force-balance equation (Eq. 7) and the expression for the total PF (Eq. 30), we obtained the following differential equation for the slow-timescale plasma density redistribution along the geomagnetic field lines:

$$\frac{d\bar{n}}{dx_\parallel} = \frac{C_g\bar{g}_\parallel(x_\parallel)\bar{n} + \nu^2\Phi_1(x_\parallel,\beta_{\kappa 0})\bar{n}^{1/2} + \nu^2\Phi_2(x_\parallel,\beta_{\kappa 0})\bar{n}^{3/2}}{\beta_{\kappa 0} + \nu^2\Phi_3(x_\parallel,\beta_{\kappa 0})\bar{n}^{-1/2} + \nu^2\Phi_4(x_\parallel,\beta_{\kappa 0})\bar{n}^{1/2}}, \tag{31}$$

where the functions $\Phi_i(x_\parallel,\beta_{\kappa 0})$ are given by

$$\Phi_1(x_\parallel,\beta_{\kappa 0}) = (A_1(x_\parallel) + A_7(x_\parallel)) + \beta_{i0\kappa}\,(A_2(x_\parallel) + A_8(x_\parallel))\,, \tag{32}$$

$$\Phi_2(x_\parallel,\beta_{\kappa 0}) = \beta_{\kappa 0}\,(A_3(x_\parallel) + A_9(x_\parallel))\,, \tag{33}$$

$$\Phi_3(x_\parallel,\beta_{\kappa 0}) = -\,(A_4(x_\parallel) + \beta_{\kappa 0}A_5)\,, \tag{34}$$

$$\Phi_4(x_\parallel,\beta_{\kappa 0}) = -\beta_{\kappa 0}A_6(x_\parallel). \tag{35}$$

In the cold-plasma limit ($\beta_{\kappa 0} \to 0$), our results differ from those of Guglielmi et al. (1999). While their approach restricted thermal effects solely to the pressure term, our general model incorporates the plasma beta into the pressure and the PF. Therefore, taking $\beta_{\kappa 0} \to 0$ in our framework removes the macroscopic fluid pressure and the thermal corrections to the PF. This reduces the system to a strict equilibrium between the gravity force and the cold PF. Then, for a cold plasma, we obtained that

$$\frac{d\bar{n}}{dx_\parallel} = \left(\frac{C_g}{\nu^2}\right)\frac{\bar{g}_\parallel(x_\parallel)}{\Phi_3(x_\parallel,0)}\bar{n}^{3/2} + \frac{\Phi_1(x_\parallel,0)}{\Phi_3(x_\parallel,0)}\bar{n}. \tag{36}$$

When gravity is weak compared to the PF, that is, $(C_g/\nu^2)(\bar{g}_\parallel\bar{n}^{1/2}/\Phi_1) \ll 1$, we can still obtain an equilibrium for the density, given by

$$\frac{d\bar{n}}{dx_\parallel} = \frac{\Phi_1(x_\parallel,0)}{\Phi_3(x_\parallel,0)}\bar{n}. \tag{37}$$

Therefore, according to our differential equation, in a cold plasma in equilibrium along the geomagnetic field lines with a strong PF compared to the effect of gravity, we have that the density satisfies the following relation:

$$\bar{n} = \exp\left(\int_0^{x_\parallel}\frac{\Phi_1(s,0)}{\Phi_3(s,0)}ds\right). \tag{38}$$

In this case, there is an equilibrium between the spatial term of the PF and the MMP term. This solution resembles the form of the non-PF solution, but instead of having the gravity acceleration inside the integral, it has $\Phi_1(x_\parallel,0)/\Phi_3(x_\parallel,0)$ as is clear by comparing Equation (38) with the $\nu = 0$ solution,

$$\bar{n} = \exp\left(\frac{C_g}{\beta_{\kappa 0}}\int_0^{x_\parallel}\bar{g}_\parallel(s)ds\right). \tag{39}$$

We analyzed the ordinary differential equation (ODE) behavior with respect to its parameters. Following the procedure in Guglielmi et al. (1999), it is useful to study the nullclines to determine the extreme values of the density and whether they correspond to minima or maxima. Considering $dn/dx_{\parallel} = 0$ in Eq. (31), we obtained that the nullcline $n_c(x_{\parallel})$ (i.e., the possible values for extrema of the solution) is given by

$$n_c(x_{\parallel}) = \left(\frac{C_g}{\nu^2}\right)^2 \frac{\bar{g}_{\parallel}^2}{4\Phi_2^2} \left\{ \sqrt{1 - \left(\frac{C_g}{\nu^2}\right)^{-2} \frac{4\Phi_1\Phi_2}{\bar{g}_{\parallel}^2}} - 1 \right\}^2 . \tag{40}$$

For a minimum of the geomagnetic field at the equator, as in a dipolar model of the magnetosphere, the ODE for the density also has a nullcline at $x_{\parallel} = 0$. The character of the solution depends on whether the nullcline is above or below the initial condition $\bar{n} = 1$ for $x_{\parallel} = 0$, and on the sign of $d\bar{n}/dx_{\parallel}$ below and above the nullcline, and on the characteristics of its slope. Therefore, it is useful to calculate the critical value of $\Lambda = \nu^2/C_g$ as a function of $\bar{\omega}$ and $\beta_{\kappa 0}$ for which the nullcline at $x_{\parallel} = 0$ coincides with the initial condition, that is, $n_c(x_{\parallel} = 0) = \bar{n}(x_{\parallel} = 0) = 1$. Λ quantifies the relative effect of gravity compared to the PF in the density redistribution. To perform a specific analysis of the nullclines, we first specified a particular geomagnetic field model. First, we defined

$$\xi_1 = \lim_{x_{\parallel}\to 0} \frac{\bar{g}_{\parallel}}{2\Phi_2}, \tag{41}$$

$$\xi_2 = \lim_{x_{\parallel}\to 0} \frac{\bar{g}_{\parallel}}{2\sqrt{-\Phi_1\Phi_2}} . \tag{42}$$

Then, we obtained that the critical value Λ_c that has to reach Λ for the nullcline to match the initial condition at $x_{\parallel} = 0$ is given by

$$\Lambda_c(\bar{\omega}, \beta_{\kappa 0}) = \frac{2\xi_1}{(\xi_1/\xi_2)^2 - 1} , \tag{43}$$

from which it is straightforward to calculate that

$$\xi_1(\bar{\omega}, \beta_{\kappa 0}) = \frac{1}{\beta_{\kappa 0}} \left[\frac{4(1-\bar{\omega})^4}{\bar{\omega}(1/2-\bar{\omega})}\right] \left(\frac{\bar{\nabla}_{\parallel}\bar{g}_{\parallel}\big|_{x_{\parallel}=0}}{\bar{\nabla}_{\parallel}^2 \mathcal{B}\big|_{x_{\parallel}=0}} \right), \tag{44}$$

and

$$\xi_2(\bar{\omega}, \beta_{\kappa 0}) = \left[\beta_{\kappa 0}\left(1 - \beta_{\kappa 0}\frac{\bar{\omega}}{4(1-\bar{\omega})^3}\right)\right]^{-1/2} \times \left[\frac{4(1-\bar{\omega})^{5/2}}{\bar{\omega}^{1/2}(2-\bar{\omega})^{1/2}(1/2-\bar{\omega})^{1/2}}\right] \left(\frac{\bar{\nabla}_{\parallel}\bar{g}_{\parallel}\big|_{x_{\parallel}=0}}{\bar{\nabla}_{\parallel}^2 \mathcal{B}\big|_{x_{\parallel}=0}} \right). \tag{45}$$

6.2. Dipolar model for the geomagnetic field

We did not assume any particular geomagnetic field model so far. As a first approach, we considered the simple case of a dipolar magnetic field centered at the planet and directed along $\hat{\mathbf{z}}$. Then,

$$\mathcal{B}_r = 2L^3 \left(\frac{1}{\bar{r}}\right)^3 \cos\theta, \tag{46}$$

$$\mathcal{B}_\theta = L^3 \left(\frac{1}{\bar{r}}\right)^3 \sin\theta, \tag{47}$$

and

$$\mathcal{B} = L^3 \left(\frac{1}{\bar{r}}\right)^3 \sqrt{1 + 3\cos^2\theta}, \tag{48}$$

with $\mathcal{B}_r = \hat{\mathbf{r}} \cdot \langle \mathbf{B} \rangle$ and $\mathcal{B}_\theta = \hat{\theta} \cdot \langle \mathbf{B} \rangle$, where $\bar{r} = r/R_p = L\sin^2\theta$ is the normalized radius with respect to the planet radius, θ is the polar angle, and L is the L-shell parameter (McIlwain 1961). Then, $\bar{r}(x_{\parallel} = 0) = L$ and $\theta(x_{\parallel} = 0) = \pi/2$. Therefore, considering the above expressions and that $\mathbf{g} = GM_p/r^2\hat{\mathbf{r}}$, we obtained $\bar{g}_{\parallel}$ and $\mathcal{B}$ as functions of the polar angle along a certain magnetic field line defined by the parameter L, with

$$\bar{g}_{\parallel}(\theta) = -\frac{1}{L^2 \sin^4\theta} \frac{2\cos\theta}{\sqrt{1+3\cos^2\theta}}, \tag{49}$$

$$\mathcal{B}(\theta) = \frac{\sqrt{1+3\cos^2\theta}}{\sin^6\theta}. \tag{50}$$

$$\frac{d}{dx_{\parallel}} = \frac{d\theta}{dx_{\parallel}}\frac{d}{d\theta} = \frac{1}{L\sin\theta\sqrt{1+3\cos^2\theta}}\frac{d}{d\theta}. \tag{51}$$

We solved the differential equation (Eq. 31) to obtain the plasma density redistribution along the geomagnetic field lines using these expressions.

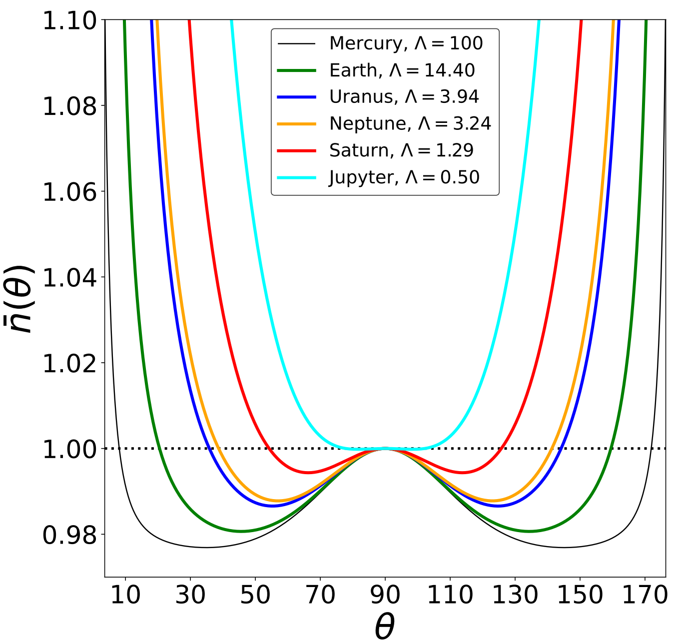

Fig. 1. Normalized density redistribution along the geomagnetic field lines as a function of the latitude for different values of Λ depending on the planet for $\nu = 0.1$, $\bar{\omega} = 0.1$, $L = 2$, $c/c_{A0} = 10^3$, $\beta_0 = 0.1$, and a Maxwellian distribution.

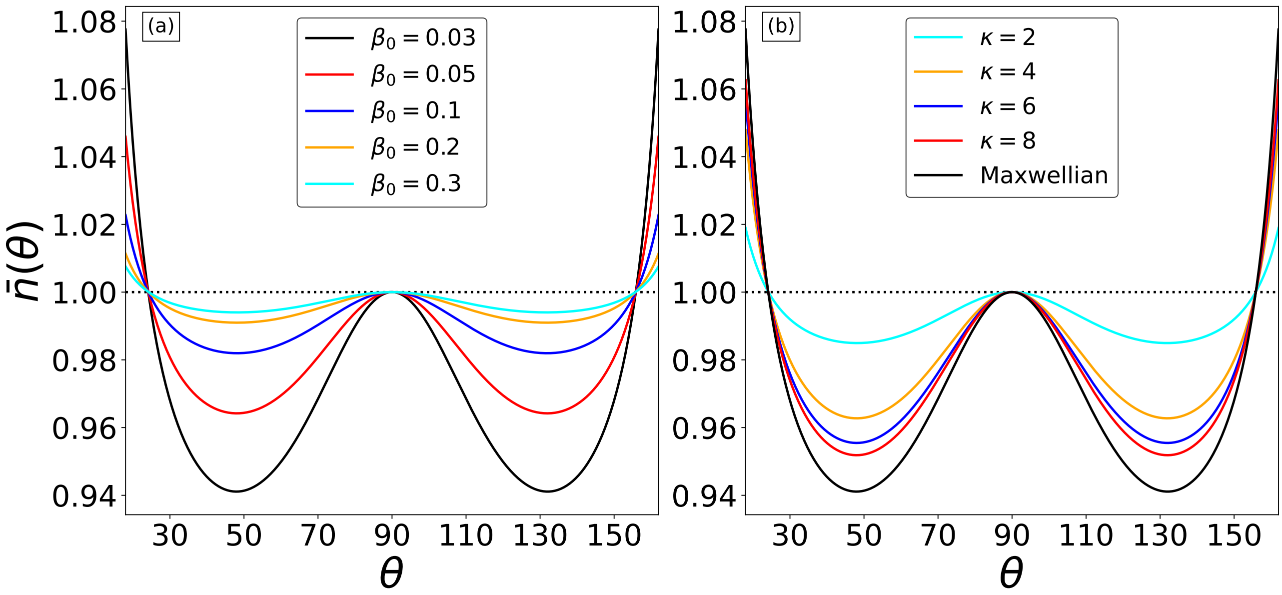

Fig. 2. Normalized density redistribution along the geomagnetic field lines as function of the colatitude for $\nu = 0.1$, $\bar{\omega} = 0.1$, $L = 2$, $c/c_{A0} = 10^3$, and for (a) different values of β_0 with a Maxwellian distribution and (b) different values of κ, with $\beta_0 = 0.03$.

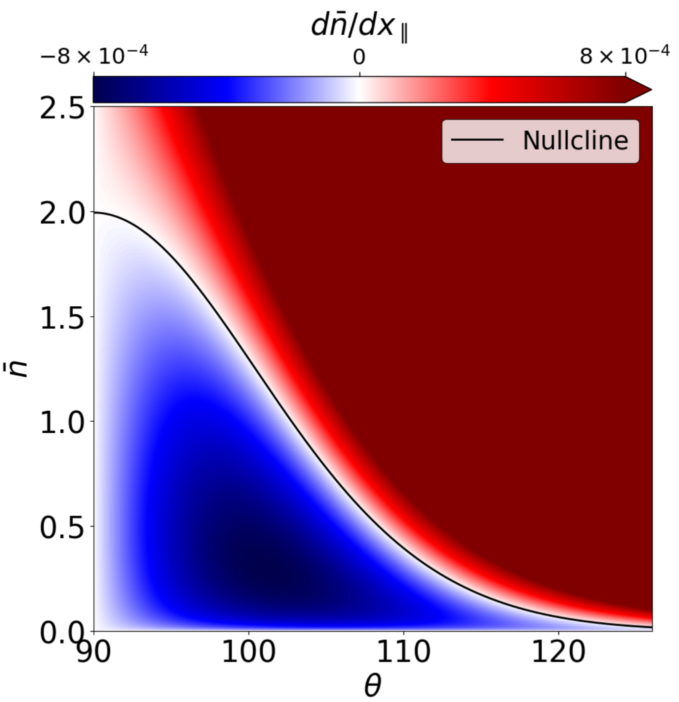

Fig. 3. Shaded isocontours of $d\bar{n}/d\bar{x}_\parallel$ as a function of the colatitude and the normalized density with the nullcline n_c represented with the black curve; with $\nu = 0.1$, $\bar{\omega} = 0.1$, $c/c_{A0} = 10^3$, $\beta_{i0\kappa} = 0.1$, $L = 2$, and the C_g of Earth.

6.3. Numerical solutions

In this section, we analyze the numerical solutions of the differential equation (Eq. 31) and their behavior for different values of $\beta_{\kappa 0}$, L, and $\bar{\omega}$. To solve the ODE describing plasma density redistribution along geomagnetic field lines, we used a fourth-order Runge-Kutta method (Butcher 1996) in the presence of a dipolar magnetic field. Since the dipolar geomagnetic field model is more appropriate for the plasmasphere, we considered low L values.

Table 1. Parameters used to calculate C_g for each planet.

Planet	R_p[m]	M_p[kg]	C_g
Mercury	$2.44 \cdot 10^6$	$3.30 \cdot 10^{23}$	$1.00 \cdot 10^{-4}$
Earth	$6.38 \cdot 10^6$	$5.97 \cdot 10^{24}$	$6.94 \cdot 10^{-4}$
Jupiter	$6.99 \cdot 10^7$	$1.90 \cdot 10^{27}$	$2.01 \cdot 10^{-2}$
Saturn	$5.44 \cdot 10^7$	$5.68 \cdot 10^{26}$	$7.75 \cdot 10^{-3}$
Uranus	$2.54 \cdot 10^7$	$8.68 \cdot 10^{25}$	$2.54 \cdot 10^{-3}$
Neptune	$2.46 \cdot 10^7$	$1.02 \cdot 10^{26}$	$3.08 \cdot 10^{-3}$

Notes. We considered $c/c_{A0} = 10^3$, where the planetary radius R_p is in meters [m], and the planetary mass M_p is in kilograms [kg].

Figure 1 shows the plasma density redistribution as a function of colatitude for $\nu = 0.1$ and different values of C_g, depending on the mass and radius of each planet in the Solar System with a magnetosphere. We used $\nu = 0.1$ as an upper limit of typical observed wave amplitudes to illustrate this PF effect. A detailed study of the ν dependence is given in section 7. The parameters for each planet are listed in Table 1. In this figure, we use the same plasma parameters for all planets to highlight the effect of gravity relative to the PF due to suprathermal particles instead of focusing on the specific characteristics of each planetary magnetosphere. This approach allowed us to maintain a certain generality in the discussion. We considered low-temperature plasmas with $\beta_{\kappa 0} = 0.1$, and Alfvén velocity of $c/c_{A0} = 10^3$, and a low L-shell parameter $L = 2$. Although these parameters do not necessarily represent typical magnetospheric values for each region of each planet, they can be applied across a wide range of zones in different planetary magnetospheres. For instance, the inner magnetosphere in Jupiter extends to $L \sim 10$, with the plasma beta mostly below ~ 0.2 due to the strong background magnetic field and low temperatures of the torus plasma region produced by the moon Io (Khurana et al. 2004). Nevertheless, the ion and electron plasma beta increase with L in the inner Jovian magnetosphere, ranging from $\beta \sim 0.01$ to $\beta \sim 1$ (Mauk et al. 1996). For Saturn, data from Pioneer 11 and Voyager 1 and 2 indicate that the inner magnetosphere extends to $L \sim 4$, with cold

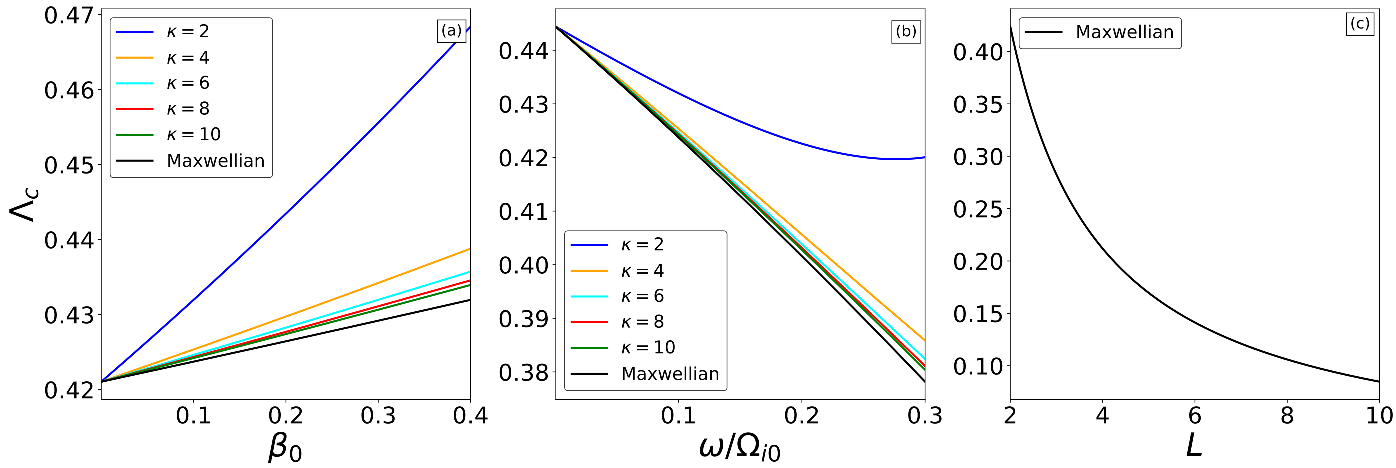

Fig. 4. Critical value Λ_c for different values of the kappa parameter as a function of (a) the plasma beta β_0, with $\bar{\omega} = 0.1$ and $L = 2$; (b) the normalized frequency ω/Ω_{i0}, with $\beta_0 = 0.1$ and $L = 2$; and (c) the L-shell parameter L, with $\beta_0 = 0.1$ and $\bar{\omega} = 0.1$. In panel (c), only the Maxwellian case is displayed, as the curves for other κ values overlap and are omitted for clarity.

plasma characterized by $\beta < 1$ (Schardt 1983). The ice giants, Uranus and Neptune, exhibit similar magnetospheric properties, both being at large heliocentric distances and occupying different regions of parameter space compared to the inner planets in the Solar System (Arridge & Paty 2021). The low-beta approximation is particularly valid in their magnetospheres because they are both very tenuous, with plasma beta values lower than those of Jupiter and Saturn. Within the magnetospheres of Uranus and Neptune, Voyager 2 a plasma beta of $\beta \sim 0.1$ at most (for $L < 15$) and $\beta \sim 0.2$, respectively (Krimigis et al. 1986, 1989).

Figure 1 shows that plasma density exhibits a local maximum instead of reaching a minimum at the equator (as expected in the absence of the PF). This indicates that the PF produces an equatorial plasma concentration that decreases with colatitude, reaches a minimum, and then increases again as it approaches the planetary surface. These solutions have the same qualitative shape as those obtained with the cold PF studied in Guglielmi et al. (1999). Therefore, the finite-temperature correction to the PF does not change the qualitative behavior of the solutions predicted in previous works. The density minimum is more pronounced for low-mass-density planets such as Mercury or Earth (i.e., for larger Λ). For instance, in the Mercury dipolar magnetosphere approximation with $L = 2$, $\beta_0 = 0.1$, $\omega/\Omega_{i0} = 0.1$, $\nu = 0.1$, and $c/c_{A0} = 10^3$, latitudes of ~ 60 degrees exhibit a $\sim 2\%$ decrease in density relative to the equator. In these high-Λ cases, the PF dominates gravity near the equator, whereas for denser planets such as Jupiter, gravity dominates, and the density minimum has a higher value. When Λ is sufficiently small, the PF is no longer able to concentrate plasma at the equator, and the density exhibits a minimum at the equator with a monotonic increase toward higher colatitudes, resembling qualitatively the standard solution without the PF effect ($\nu = 0$) given in Equation (39).

Panels (a) and (b) of Figure 2 show the normalized plasma density redistribution as a function of the colatitude θ. Panel (a) evaluates the density for different values of the plasma beta β_0 for a Maxwellian distribution with $L = 2$, $c/c_{A0} = 10^3$, $\nu = 0.1$, and $\bar{\omega} = 0.1$. This panel shows that the magnitude of the density minimum decreases with increasing plasma beta. Therefore, our model predicts that PF effects on density redistribution along geomagnetic field lines decrease as plasma temperature increases. A similar trend can be expected as the kappa parameter decreases. The kappa parameter can significantly suppress the density accumulation at the equator, as shown in panel (b) of Figure 2, where the plasma density is plotted as a function of colatitude for different values of κ with $\beta_0 = 0.03$, $L = 2$, $c/c_{A0} = 10^3$, $\nu = 0.1$, and $\bar{\omega} = 0.1$. As shown in this panel, for $\kappa = 2$, the equatorial density increase is lower than 2% compared to the 6% observed in the Maxwellian case. Hence, the PF effect is less pronounced for plasmas with suprathermal distributions. This behavior can be understood by noting that as plasma beta increases or the kappa parameter decreases, the plasma pressure increases, counteracting the PF tendency to concentrate plasma at the equator. Conversely, when the plasma beta decreases, the PF can concentrate more plasma at the equator, producing steeper spatial density variations. For very low plasma beta, the slow-scale density no longer varies smoothly in space, and the WKB approximation is invalid.

These results highlight the importance of including nonthermal correction in the PF because measurements of velocity distributions in planetary magnetospheres are often well fitted by Kappa distributions to describe their suprathermal tails (Lazar & Fichtner 2021). For example, Cassini measurements at Jupiter near the equator for radial distances with $L \sim 6 - 46$ (Mauk et al. 1996) indicated that a modified Kappa distribution accurately represents ions. This distribution has two spectral indices, and at high energies, a power law is recovered with an effective spectral index equal to the sum of the two indices. With this sum, the kappa parameter can be considered in the range $\sim 2 - 4$. In Saturn, ion spectra are well fitted by a Kappa distribution with $\kappa \sim 6 - 8$ at radial distances with $L \sim 6 - 20$ (Schardt 1983; Dialynas et al. 2009). Therefore, the Jupiter and Saturn magnetospheres exhibit significant suprathermal properties, which, under our approximations, are predicted to highly reduce the plasma confinement near the equator. As shown in panel (b) of Figure 2, lower values of κ lead to a broader latitudinal distribution, effectively redistributing the plasma density away from the equatorial plane. In the case of the ice giants, Voyager 2 measurements revealed nonthermal ion and electron spectra at Uranus (Krimigis et al. 1986; Mauk et al. 1987), well modeled as a Maxwellian core with high-energy power-law tails (with exponents between 3 and 10). For Neptune, Voyager 2 data (Krimigis et al. 1989) indicated that Triton affects the outer magnetosphere: inside the satellite orbit ($L \sim 14$), the proton spectrum is Maxwellian, whereas outside, it presents nonthermal properties and is modeled with a power-law distribution (with exponent ~ 4). Despite

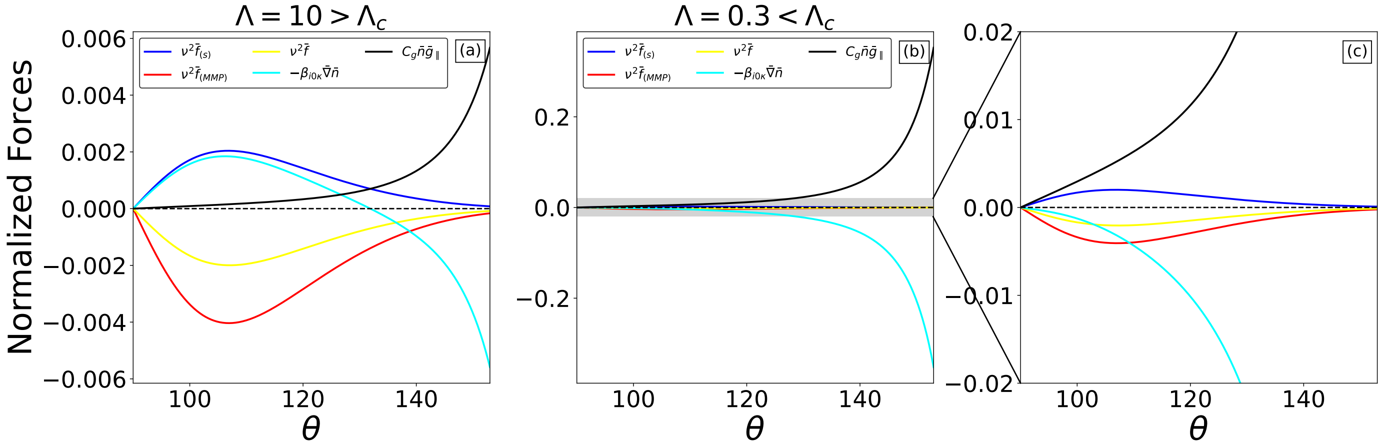

Fig. 5. Panels (a)-(b): Normalized forces that act on the equilibrium Equation (7) as a function of the colatitude θ with $\nu = 0.1$, $\bar{\omega} = 0.1$, $c/c_{A0} = 10^3$, $\beta_{i0\kappa} = 0.1$, and $L = 2$ for (a) $\Lambda = 10 > \Lambda_c$ and (b) $\Lambda = 0.3 < \Lambda_c$. Panel (c): Zoom over the gray shaded region in panel (b).

being modeled with a power law, the high-energy tails of Uranus and Neptune are consistent with Kappa distributions (Lazar & Fichtner 2021). Therefore, we expect that nonthermal properties in the planetary magnetospheres of the Solar System counteract the tendency of the PF to accumulate plasma at the equator in the dipolar magnetic field approximation. For more complex realistic magnetosphere geometries, particularly the non-dipolar field of Neptune and Uranus (Arridge & Paty 2021) and non-dipolar regions of the terrestrial magnetosphere, plasma accumulation due to the PF is expected to occur at local minima of the geomagnetic field, consistent with Nekrasov & Feygin (2016) using the Antonova & Shabanskii (1968) magnetic field model of the Earth's dayside magnetosphere. Their study found density enhancements at local geomagnetic minima. We justify this point in more detail below.

To further understand the behavior of the solutions, we analyzed their nullclines. Thus, we analyzed the properties of $d\bar{n}/dx_\parallel$, with the particular case of the dipolar geomagnetic field model. Figure 3 shows shaded isocontours of $d\bar{n}/dx_\parallel$ as a function of colatitude and the normalized density, with the nullcline of Equation (40) represented with the black curve; with $\nu = 0.1$, $\bar{\omega} = 0.1$, $c/c_{A0} = 10^3$, $\beta_{i0\kappa} = 0.1$, $L = 2$ and the C_g of Earth. We focus on $\theta > \pi/2$, due to symmetry about the equator. Above the nullcline, the spatial derivative of the density is positive $d\bar{n}/dx_\parallel > 0$; below, it is negative $d\bar{n}/dx_\parallel < 0$, with the nullcline having a negative slope. Hence, if the nullcline is below the initial condition at $x_\parallel = 0$, the density increases monotonically with colatitude, exhibiting a minimum at the equator. Conversely, if the nullcline lies above the initial condition, the density decreases until it crosses the nullcline, and it then increases indefinitely. For $\Lambda > \Lambda_c$, with Λ_c defined in Equation (43), we have that $n_c(x_\parallel = 0) < 1$, and there is a maximum at the equator and two symmetrical minima around it. On the other hand, for $\Lambda < \Lambda_c$, then $n_c(x_\parallel = 0) > 1$, and the plasma density only has a minimum located at the equator. The critical value Λ_c depends on the plasma beta, kappa, the frequency, and the L-shell parameter. Consequently, as in the cold PF case studied by Guglielmi et al. (1999), the density closely resembles a second-kind phase transition.

Panels (a)-(c) of Figure 4 show the critical value Λ_c as a function of the plasma beta, the frequency, and the L-shell parameter for different kappa values. In panel (a) (with $L = 2$, $\bar{\omega} = 0.1$), Λ_c increases approximately linearly with the plasma beta in low-beta regimes, reaching $\Lambda_c \sim 0.42$ for cold plasmas. The increase is steeper for nonthermal plasmas. Panel (b) (with $L = 2$, $\beta_0 = 0.1$ and $\kappa \geq 4$) shows a linear decrease in Λ_c with frequency, with a higher decline ratio for Maxwellian plasmas. For extremely nonthermal plasmas with $\kappa \sim 2$, Λ_c decreases, reaching a minimum, then increases near $\omega/\Omega_{i0} \sim 0.3$. Panel (c) (with $\bar{\omega} = 0.1, \beta_0 = 0.1$) shows a decrease in Λ_c with the L-shell parameter, with a stronger variation compared to plasma beta and frequency. Λ_c can reach values of ~ 0.1 for $L \sim 10, \beta = 0.1$, and $\omega/\Omega_{i0} = 0.1$. However, since the dipole geomagnetic field model is generally more accurate near the plasmasphere, these results should be better adjusted for low L values, depending on the planet. Moreover, the variation in Λ_c with L is almost independent of kappa; hence, only the Maxwellian case is displayed because the curves for other κ values overlap and are omitted for clarity.

Finally, to understand the underlying physics, we examined the forces involved in the equilibrium along geomagnetic field lines above and below Λ_c. Panels (a)-(b) of Figure 5 show the normalized forces that act in the equilibrium equation (Eq. 7) as a function of the colatitude for $\Lambda > \Lambda_c$ and $\Lambda < \Lambda_c$, respectively. Panel (c) shows a zoom over the gray shaded region in panel (b). From inspecting Equation (28), since $\partial\varepsilon/\partial\mathcal{B} < 0$ for EMIC waves in low-beta regimes, the MMP force pushes the plasma against the gradient of the geomagnetic field, that is, it tends to concentrate the plasma toward the equator. Consequently, in complex geometries, the MMP force might push the plasma to the local minima of the geomagnetic field, which is consistent with previous studies (Lundin & Hultqvist 1989; Guglielmi & Lundin 2001b; Nekrasov & Feygin 2012b, 2016). On the other hand, the wave amplitude, which is $\propto B/n^{1/4}$ for our WKB approximation, increases with colatitude due to the rising magnetic field magnitude and the decreasing density (pushed equatorward by the MMP force). Then, the spatial PF term, directed along the wave-amplitude gradient, drives plasma toward the planetary surface. Despite this, MMP dominates, as shown in panels (a) and (c) of Figure 5, where the sum of the spatial and MMP terms of the normalized PF $\nu^2\bar{f}$ is negative, directing plasma equatorward. For $\Lambda > \Lambda_c$, gravity is negligible near the equator compared to the PF, as shown in panel (a) of Figure 5. Therefore, the PF tendency to concentrate plasma towards the equator overcomes the gravity tendency to push it to the planetary surface, with the pressure equilibrating the PF. As colatitude increases, gravity increases in magnitude until it overcomes the PF, which decreases with colatitude (since it is inversely proportional to the magnetic field magnitude), thereby increasing the density toward the surface. For $\Lambda < \Lambda_c$, gravity dominates everywhere, even closer to the equator, as shown in panel (c) of Figure 5, pushing plasma planetward, balanced by the pressure.

7. Dependence on the wave amplitude and average magnetospheric conditions

We analyzed the magnitude of the ponderomotive effect dependence on the relative wave amplitude, ν, and average conditions across the magnetospheres of Earth, Jupiter, and Saturn. Our analysis was grounded in statistical observational values of ν and plasma parameters, restricting the spatial domain to the dayside, where EMIC waves are frequent and the magnetic field approximates a dipole. We focused on cold plasma regions ($\beta_0 < 0.3$), corresponding to the inner magnetospheres: $2.25 \leq L \leq 8$ (Earth), $5 \leq L \leq 10$ (Jupiter), and $3.6 \leq L \leq 7$ (Saturn).

To evaluate the PF density redistribution, Figure 6 displays the numerically computed $\Delta n/n_0 = (n_0 - n_{\min})/n_0$ as a function of L and ν, where $n_{\min}$ is the minimum density. This quantity indicates plasma accumulation at the equator due to the PF. Values $\Delta n/n_0 > 0.2$ are shown for context, but exceed the validity of our perturbative model. We assumed a Maxwellian velocity distribution for simplicity. We adopted $\bar{\omega} = 0.1$ for Earth and $\bar{\omega} = 0.3$ for Jupiter and Saturn to account for the commonly observed EMIC frequency bands (see below). As detailed in Appendix B, which also outlines the empirical background profiles (B_0, c_{A0}/c, β_0) used to compute $n_{\min}$, the background gyrofrequency Ω_0 was set to $1\,\Omega_{H^+}$ for Earth, $6.40\times10^{-2}\,\Omega_{H^+}$ for Jupiter, and $6.55\times10^{-2}\,\Omega_{H^+}$ for Saturn to account for ion composition.

7.1. Ponderomotive effect at Earth's inner magnetosphere

Figure 6 a shows density accumulation increases with wave amplitude. The L-shell dependence is governed by plasma beta, which counteracts the PF effect and scales with the local Alfvén speed ratio as $\nu^2/C_g \propto (c_{A0}/c)^2$. Thus, $\Delta n/n_0$ decreases significantly at low c_{A0}/c values. The abrupt variation near $L \sim 5$ reflects the plasmapause density gradient.

During quiet geomagnetic conditions, prevalent EMIC He^+ band emissions ($\omega < 0.25\Omega_{H^+}$, mainly found at $4 \leq L \leq 6$ in prenoon and afternoon sectors) typically exhibit relative amplitudes of $\nu \sim 0.001 - 0.01$ (Saikin et al. 2015; Usanova et al. 2014). Consequently, the PF density perturbation is negligible ($\Delta n/n_0 < 10^{-4}$). However, extreme solar wind compressions can trigger high-amplitude Pc1 emissions ($\nu \sim 0.01 - 0.07$) in the dawn and noon sectors spanning $L = 4 - 5.7$ (Engebretson et al. 2015), potentially leading to a non-negligible accumulation of plasma ($\Delta n/n_0 \sim 10^{-2}$).

We extrapolated this to higher L-shells ($L > 6$) to evaluate qualitative trends, although a rigorous treatment requires extending the model to account for non-dipolar geometries (Antonova & Shabanskii 1968; Nekrasov & Feygin 2015). In these outer regions, high-amplitude EMIC waves are commonly observed (Min et al. 2012). Dusk-sector emissions are dominated by the He^+ band ($L = 8 - 12$, $\nu \sim 0.01 - 0.1$), theoretically yielding a relative maximum of $\Delta n/n_0 \gtrsim 10^{-2}$. Conversely, dawn-sector waves are dominated by the H^+ band with lower amplitudes ($\nu \sim 0.01$), but higher normalized frequencies ($\omega \sim 0.5\Omega_{H^+}$), approaching the proton-cyclotron resonance. Since our current low-frequency formalism fails in this regime, this motivates future high-frequency model extensions, where we expect the PF to be stronger.

7.2. Ponderomotive effect at Jupiter's inner magnetosphere

Figure 6 b shows that Jupiter's inner magnetosphere requires high wave amplitudes ($\nu > 10^{-2}$) for the PF to redistribute plasma toward the equator. This results from low c_{A0}/c values (7×10^{-4} to 2×10^{-3}) caused by massive heavy-ion mass-loading from the Io plasma torus (Bagenal 1994; Saur et al. 2004). Within this high-density region ($L \sim 5.9$), where EMIC waves are predominantly observed near the downstream region of the plasma torus, the strong background magnetic field restricts relative EMIC wave amplitudes to $\nu \lesssim 0.05$ (Cao et al. 2025; Blanco-Cano et al. 2001), effectively canceling the PF under typical conditions. However, substantial density redistribution ($\Delta n/n_0 \sim 10^{-1}$) can emerge during exceptionally high-amplitude events ($\nu > 0.08$) in the torus or farther outward ($L \sim 8$) before the local plasma beta increases. The observed wave power spectra are typically centered around the SO^+ gyrofrequency ($\Omega_{SO^+} \sim 0.33\,\Omega_0$) and extend to the S^+ gyrofrequency ($\Omega_{S^+} \sim 0.49\,\Omega_0$) (Blanco-Cano et al. 2001); hence, our choice of a normalized frequency, $\bar{\omega} = 0.3$, appropriately represents the frequency bands of Jovian EMIC waves.

While our spatial domain is restricted to $L \leq 10$, where the low-beta plasma and dipole approximations hold (Connerney et al. 1981), the middle and outer magnetosphere ($L > 10$) present a physically interesting regime. Observations in these highly distorted high-beta regions reveal dawn-side EMIC waves with exceptionally large relative amplitudes of $\nu \sim 0.1 - 0.25$ (Yao et al. 2021; Yuan et al. 2024). This suggests that the Jovian outer magnetosphere frequently operates in a highly nonlinear regime where the PF is expected to exert a substantial force against the background magnetic field gradient. A stronger PF interaction is also expected near heavy-ion resonances, strongly motivating future high-frequency model extensions.

7.3. Ponderomotive effect at Saturn's inner magnetosphere

Figure 6 c shows that Saturn's inner magnetosphere ($3.6 \leq L \leq 7$), where the magnetic field remains approximately dipolar (André et al. 2008), also requires high wave amplitudes ($\nu > 0.04$) for the PF to redistribute plasma. This environment features even lower c_{A0}/c values (1×10^{-4} to 8×10^{-4}) than Jupiter due to weak magnetic fields and high concentrations of heavy water-group ions (O^+, OH^+, H_2O^+, and H_3O^+) sourced by the active cryovolcanism of Enceladus (Meeks et al. 2016). Combined with the rapid increase in the plasma beta (see B.3.c), this demands higher ν values for the PF to act at larger L-shells, completely suppressing the PF redistribution for $L \gtrsim 6$ and $\nu < 0.1$.

An equatorial statistical study by Meeks et al. (2016) showed continuous EMIC wave occurrence between the orbits of Enceladus and Dione, exhibiting a steep decay toward the Rhea orbit ($L = 8.74$) correlated with the radial decrease in water-group ion density. This study reported frequencies between $0.5 - 2.0\,\Omega_{H_2O^+}$ with a peak close to $\Omega_{H_2O^+}$, corresponding to roughly $0.42 - 1.70\,\Omega_0$. We therefore set our normalized frequency to $\bar{\omega} = 0.3$, which is at the upper limit of what our low-frequency approximation can hold. Observational amplitudes yield typical relative values of $\nu \sim 0.004 - 0.02$ (Meeks et al. 2016; Long et al. 2022). According to Figure 6 c, the PF effect is canceled under these typical conditions. However, significant density redistribution ($\Delta n/n_0 \gtrsim 10^{-1}$) might emerge during exceptional high-amplitude events ($\nu > 0.07$) near the Enceladus orbit ($L \sim 3.95$), where EMIC waves have their highest occurrence rate. In addition, since wave frequencies are frequently close to the water-

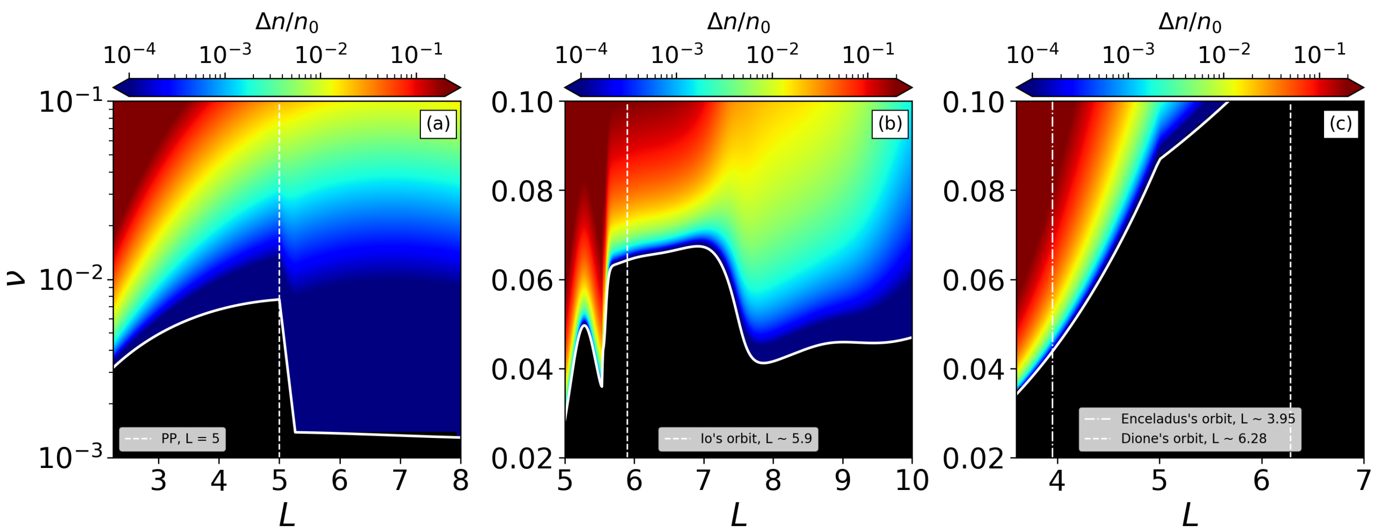

Fig. 6. Shaded isocontours of the relative difference between the equatorial and minimum densities, $\Delta n/n_0 = (n_0 - n_{\min})/n_0$ (log scale), as a function of L-shell (L) and relative wave amplitude (ν) under typical plasma conditions. (a) Earth's inner magnetosphere, where the vertical dashed white line denotes the plasmapause (PP). Here, ν is denoted on a log scale. (b) Jupiter's inner magnetosphere, with the Io orbit marked by a vertical dashed white line. (c) Saturn's inner magnetosphere, with vertical white lines indicating the orbits of Enceladus (dash-dotted) and Dione (dashed). In all panels, the solid white line represents the critical ν value associated with Λ_c, and the shaded black regions indicate $\Delta n/n_0 = 0$, indicating that the density follows the standard profile with a single minimum at the equator.

group ion resonance, an extension of our framework to higher frequencies is strongly motivated.

8. Conclusions

We have analytically studied the effects of the nonthermal properties of velocity distributions observed in different planetary magnetospheres on the field-aligned plasma density redistribution induced by PF from traveling EMIC waves with a dipole model of the geomagnetic field in a low-beta approximation. We showed that the nonlinear plasma density solution due to PF in nonthermal plasmas resembles a second-kind phase transition, consistent with previous work (Guglielmi et al. 1999). Furthermore, we calculated the variation in the critical parameter Λ_c for the phase transition with the plasma beta β, the kappa parameter κ, and the L-shell. For values above Λ_c, which would mainly depend on the wave amplitude responsible for the PF, plasma accumulation at the equator is predicted. This result is consistent with previous studies (Allan 1993; Guglielmi et al. 1999; Nekrasov & Feygin 2018), which showed an accumulation at the geomagnetic field minimum, and specifically, at the equator for a dipole geomagnetic model.

As expected in low-beta plasmas, nonthermal and finite-temperature effects do not alter the qualitative behavior of plasma redistribution. Nevertheless, we found that the effects of the Kappa distribution and plasma beta counteract plasma accumulation at the geomagnetic field minimum due to the PF. We also demonstrated that this nonlinear effect may be relevant across planetary magnetospheres in the Solar System, depending on the region and local plasma conditions. For instance, taking a low plasma beta, we found that for $\kappa = 2$, the equatorial density enhancement relative to the density minimum is lower than 2% compared to the 6% in the Maxwellian case.

These results agree with Allan & Poulter (1992), who used a box-model simulation of the Earth's magnetosphere and showed that the nonlinear plasma density enhancement induced by PF from fast magnetosonic waves increases at lower local plasma beta. In the case of the nonthermal plasmas considered here, the effect of the plasma beta is amplified by the Kappa distribution, reducing density enhancement. This result is especially relevant because the measured kappa values in planetary magnetospheres of our Solar System typically range from 2 to 10 in low-beta regions (Schardt 1983; Krimigis et al. 1986; Mauk et al. 1987; Krimigis et al. 1989; Mauk et al. 1996; Dialynas et al. 2009), which is well within the validity of our approximation. We also found that the critical parameter Λ_c for the phase transition increases linearly with plasma beta, with a steeper slope at low kappa. It decreases with frequency, though more slowly for small κ, and decreases with L-shell, with negligible dependence on κ.

We employed the simplest geomagnetic model (dipole) to maintain generality and provided broad insights into nonthermal effects on plasma redistribution due to PF. These results can be qualitatively applied to different planetary magnetospheres of our Solar System. However, each magnetosphere (and its different regions) has distinct structural characteristics that must be accounted for in specific studies. Despite this, because the MMP force associated with traveling EMIC waves pushes plasma against the magnetic field gradient, we expect this type of pulsation to contribute to plasma accumulation at magnetic minima in more complex geometries as well, in agreement with Nekrasov & Feygin (2018).

By applying this model to the dayside low-beta inner magnetospheric regions of Earth, Jupiter, and Saturn, we demonstrated that the PF drives substantial equatorial density accumulation ($\Delta n/n_0 \sim 10^{-2} - 10^{-1}$) during exceptionally high-amplitude EMIC events ($\nu \sim 0.1$). These findings strongly motivate an extension of our framework to regions where the MHD approximation breaks down and nonthermal or multicomponent plasma effects dominate. Specifically, the high-beta collisionless environments of the terrestrial and Jovian outer magnetospheres frequently exhibit nonthermal distributions (Kane et al. 1995; Pierrard & Stegen 2008; Kirpichev et al. 2021) and highly nonlinear wave amplitudes ($\nu \gtrsim 10^{-1}$). Moreover, since standard time-averaged statistics underestimate the peak intensity of short wave-packets (Shi et al. 2024), this mechanism's impact likely exceeds current estimates. Additionally, future work will adapt this model for Mercury's magnetosphere, where ULF standing waves propagate near the ion gyrofrequency in Kappa-distributed plasmas (Othmer, C. et al. 1999; Christon 1987; Zhao et al. 2020; Harada et al. 2022), and incorporate the multi-ion near-cyclotron resonances crucial for the heavy-ion-rich inner magnetospheres of Jupiter and Saturn.

Acknowledgements. We are grateful for the support of ANID Chile through the National Doctoral Scholarships No. 21231291 (JET), and FONDECYT grants Nos. 1230094 (FAA) and 1240281 (PSM).

References

Allan, W. 1993, JGR: Space Physics, 98, 1409
Allan, W. 1994, JGR: Space Physics, 99, 21281
Allan, W., Manuel, J. R., & Poulter, E. M. 1991, JGR: Space Physics, 96, 11461
Allan, W. & Poulter, E. M. 1992, ROPP, 55, 533
Anderson, B. J., Erlandson, R. E., & Zanetti, L. J. 1992, JGR: Space Physics, 97, 3075
André, N., Blanc, M., Maurice, S., et al. 2008, Rev. Geophys., 46
Andrés, N., Gómez, D., Bertucci, C., Mazelle, C., & Dougherty, M. 2013, P&SS, 79-80, 64
Antonova, A. & Shabanskii, V. 1968, Geomagn. Aeron., 8, 801
Arridge, C. S., Khurana, K. K., Russell, C. T., et al. 2008, JGR: Space Physics, 113
Arridge, C. S. & Paty, C. 2021, Asymmetrical Magnetospheres (American Geophysical Union (AGU)), 515–534
Bagenal, F. 1994, JGR: Space Physics, 99, 11043
Bagenal, F. & Delamere, P. A. 2011, JGR: Space Physics, 116
Blanco-Cano, X., Russell, C., Strangeway, R., Kivelson, M., & Khurana, K. 2001, ASR, 28, 1469
Boardsen, S. A., Anderson, B. J., Acuña, M. H., et al. 2009a, GRL, 36
Boardsen, S. A., Slavin, J. A., Anderson, B. J., et al. 2012, JGR: Space Physics, 117
Boardsen, S. A., Slavin, J. A., Anderson, B. J., Korth, H., & Solomon, S. C. 2009b, GRL, 36
Butcher, J. 1996, Appl. Numer. Math., 20, 247
Cahill, L. & Patel, V. 1967, P&SS, 15, 997
Cao, X., Wang, S., Ni, B., et al. 2025, GRL, 52, e2025GL115547
Carpenter, D. L. & Anderson, R. R. 1992, JGR: Space Physics, 97, 1097
Chappell, C. R. 1974, JGR, 79, 1861
Christon, S. 1987, Icarus, 71, 448
Connerney, J. E. P., Acuña, M. H., & Ness, N. F. 1981, JGR: Space Physics, 86, 8370
Connerney, J. E. P., Acuña, M. H., & Ness, N. F. 1983, JGR: Space Physics, 88, 8779
De Michelis, P., Daglis, I. A., & Consolini, G. 1999, JGR: Space Physics, 104, 28615
Delamere, P. A. 2016, A Review of the Low-Frequency Waves in the Giant Magnetospheres (American Geophysical Union (AGU)), 365–378
Dialynas, K., Krimigis, S. M., Mitchell, D. G., et al. 2009, JGR: Space Physics, 114
Engebretson, M. J., Posch, J. L., Wygant, J. R., et al. 2015, JGR: Space Physics, 120, 5465
Espinoza-Troni, J., A Asenjo, F., & Moya, P. S. 2023, PPCF, 65, 065008
Espinoza-Troni, Joaquín, Asenjo, Felipe A., & Moya, Pablo S. 2024, A&A, 686, A26
Farrell, W. M., Lepping, R. P., & Smith, C. W. 1993, JGR: Space Physics, 98, 3631
Ghatak, A. K., Gallawa, R. L., & Goyal, I. C. 1991, Modified airy function and WKB solutions to the wave equation
Guglielmi, A. & Feygin, F. 2023, STP, 9, 28
Guglielmi, A., Feygin, F., & Potapov, A. 2024, JASTP, 10, 14
Guglielmi, A., Hayashi, K., Lundin, R., & Potapov, A. 1999, EPS, 51, 1297–1308
Guglielmi, A. & Lundin, R. 2001a, JGR: Space Physics, 106, 13219
Guglielmi, A. & Lundin, R. 2001b, JGR: Space Physics, 106, 13219
Guglielmi, A., Lundin, R., Potapov, A., & Tsegmed, B. 2004, in 35th COSPAR Scientific Assembly, Vol. 35, 805
Guglielmi, A. V. & Feygin, F. Z. 2018, Izv. Phys. Solid Earth, 54, 712–720
Guglielmi, A. V., Pokhotelov, O. A., Feygin, F. Z., et al. 1995, JGR: Space Physics, 100, 7997
Guglielmi, A. V., Potapov, A. S., & Feygin, F. Z. 2025, Sol. Syst. Res., 59
Harada, Y., Aizawa, S., Saito, Y., et al. 2022, GRL, 49, e2022GL100279, e2022GL100279 2022GL100279
Hartinger, M. D., Takahashi, K., Drozdov, A. Y., et al. 2022, Front. Astron. Space Sci., Volume 9 - 2022
Holme, R. & Bloxham, J. 1996, JGR: Planets, 101, 2177
Hora, H. 1969, PoF, 12, 182
Hughes, W. J. 1994, Magnetospheric ULF Waves: A Tutorial with a Historical Perspective (American Geophysical Union (AGU)), 1–11
Kane, M., Mauk, B. H., Keath, E. P., & Krimigis, S. M. 1995, JGR: Space Physics, 100, 19473
Kangas, J., Guglielmi, A., & Pokhotelov, O. 1998, SSR, 83, 435–512
Karpman, V. I. & Shagalov, A. G. 1982, JPP, 27, 215–224
Kentwell, G. & Jones, D. 1987, Phys. Rep., 145, 319
Khurana, K. K., Kivelson, M. G., Vasyliunas, V. M., et al. 2004, in Jupiter. The Planet, Satellites and Magnetosphere, ed. F. Bagenal, T. E. Dowling, & W. B. McKinnon, Vol. 1, 593–616
Kim, E.-H., Johnson, J. R., Valeo, E., & Phillips, C. K. 2015, GRL, 42, 5147
Kirpichev, I. P. & Antonova, E. E. 2020, ApJ, 891, 35
Kirpichev, I. P., Antonova, E. E., Stepanova, M., et al. 2021, JGR: Space Physics, 126, e2021JA029409, e2021JA029409 2021JA029409
Kleindienst, G., Glassmeier, K.-H., Simon, S., Dougherty, M. K., & Krupp, N. 2009, ANGEO, 27, 885
Kono, M. & Sanuki, H. 1987, JPP, 38, 43–51
Krall, N. A. & Trivelpiece, A. W. 1986, Principles of plasma physics (San Francisco Pr.)
Krimigis, S. M., Armstrong, T. P., Axford, W. I., et al. 1989, Science, 246, 1483
Krimigis, S. M., Armstrong, T. P., Axford, W. I., et al. 1986, Science, 233, 97
Krimigis, S. M., Carbary, J. F., Keath, E. P., et al. 1983, JGR: Space Physics, 88, 8871
Kwon, H.-J., Kim, K.-H., Jee, G., et al. 2015, GRL, 42, 7303
Lamb, B. M., Dimonte, G., & Morales, G. J. 1984, Phys. Fluids, 27, 1401
Lazar, M. & Fichtner, H., eds. 2021, Astrophysics and Space Science Library, Vol. 464, Kappa Distributions: From Observational Evidences via Controversial Predictions to a Consistent Theory of Nonequilibrium Plasmas (Cham: Springer International Publishing)
Lazar, M., López, R. A., Poedts, S., & Shaaban, S. M. 2023, PoP, 30, 082106
Lazar, M., Pierrard, V., Shaaban, S. M., Fichtner, H., & Poedts, S. 2017, A&A, 602, A44
Lee, N. C. & Parks, G. K. 1983, Phys. Fluids, 26, 724
Lee, N. C. & Parks, G. K. 1998, PoP, 5, 3853
Li, X. & Temerin, M. 1993, GRL, 20, 13
Long, M., Cao, X., Gu, X., et al. 2022, ApJ, 932, 56
Lundin, R. & Guglielmi, A. 2007, SSR, 127, 1
Lundin, R. & Hultqvist, B. 1989, JGR: Space Physics, 94, 6665
Lundin, R. & Lidgren, H. 2022, Cosmic implications of ponderomotive wave forces (Cambridge Scholars Publishing)
Mauk, B. H., Gary, S. A., Kane, M., et al. 1996, JGR: Space Physics, 101, 7685
Mauk, B. H., Keath, E. P., Kane, M., et al. 1991, JGR: Space Physics, 96, 19061
Mauk, B. H., Krimigis, S. M., Keath, E. P., et al. 1987, JGR: Space Physics, 92, 15283
Mauk, B. H., Mitchell, D. G., McEntire, R. W., et al. 2004, JGR: Space Physics, 109
McIlwain, C. E. 1961, JGR, 66, 3681
McNutt Jr., R. L., Belcher, J. W., & Bridge, H. S. 1981, JGR: Space Physics, 86, 8319
Mead, G. D. 1964, JGR, 69, 1181
Meeks, Z., Simon, S., & Kabanovic, S. 2016, P&SS, 129, 47
Min, K., Lee, J., Keika, K., & Li, W. 2012, JGR: Space Physics, 117
Mursula, K., Bräysy, T., Niskala, K., & Russell, C. T. 2001, JGR: Space Physics, 106, 29543
Nekrasov, A. K. & Feygin, F. Z. 2012a, ApSS, 341, 225–230
Nekrasov, A. K. & Feygin, F. Z. 2012b, ApSS, 341, 225
Nekrasov, A. K. & Feygin, F. Z. 2015, ApSS, 359
Nekrasov, A. K. & Feygin, F. Z. 2016, Geomagn. Aeron., 56, 441–447
Nekrasov, A. K. & Feygin, F. Z. 2018, Izv. Phys. Solid Earth, 54, 741–748
Orlowski, D. S., Russell, C. T., & Lepping, R. P. 1992, JGR: Space Physics, 97, 19187
Othmer, C., Glassmeier, K., & Cramm, R. 1999, JGR: Space Physics, 104, 10369
Persoon, A. M., Gurnett, D. A., Santolik, O., et al. 2009, JGR: Space Physics, 114
Petkaki, P. & Dougherty, M. K. 2001, ASR, 28, 909
Pierrard, V. & Stegen, K. 2008, JGR: Space Physics, 113
Rohatgi, A. 2024, WebPlotDigitizer: Version 4.7
Russell, C. & Lepping, R. 1992, ASR, 12, 43
Russell, C. T. 1989, GRL, 16, 1253
Saikin, A. A., Zhang, J.-C., Allen, R. C., et al. 2015, JGR: Space Physics, 120, 7477
Sarris, T. E., Wright, A. N., & Li, X. 2009, JGR: Space Physics, 114
Saur, J., Mauk, B. H., Kaßner, A., & Neubauer, F. M. 2004, JGR: Space Physics, 109
Schardt, A. W. 1983, Rev. Geophys., 21, 390
Sergis, N., Jackman, C. M., Thomsen, M. F., et al. 2017, JGR: Space Physics, 122, 1803
Shi, X., Artemyev, A., Zhang, X.-J., et al. 2024, JGR: Space Physics, 129, e2023JA032179
Sun, J. W., Xie, L., Yao, Z. H., et al. 2024, JGR: Planets, 129, e2023JE008279, e2023JE008279 2023JE008279
Tskhakaya, D. D. 1981, JPP, 25, 233–238
Usanova, M. E., Drozdov, A., Orlova, K., et al. 2014, GRL, 41, 1375
Washimi, H. & Karpman, V. I. 1976, JETP, 44, 528, aDS Bibcode: 1976JETP...44..528W
Yao, Z., Dunn, W. R., Woodfield, E. E., et al. 2021, Sci. Adv., 7, eabf0851
Yuan, Z., Zhao, Y., Yu, X., Xue, Z., & Deng, D. 2024, GRL, 51, e2024GL109691
Zhao, J.-T., Zong, Q.-G., Slavin, J. A., et al. 2020, GRL, 47, e2020GL088075, e2020GL088075 10.1029/2020GL088075

Appendix A: Ponderomotive force calculation

Appendix A.1: Spatial term

Using equations (25) and (17) and neglecting terms at the second order of the plasma beta, we obtain that

$$\bar{f}_{(s)\|} = \frac{1}{4}\left(\frac{c}{c_{A0}}\right)^{-1}\frac{(1-\bar{\omega})^{1/2}}{\varepsilon_c^{1/2}}\left\{-\frac{\alpha}{2}\left[\left(1+\frac{\delta_{\kappa 0}}{2}\right)-\frac{\delta_\kappa}{2}\right]\bar{\nabla}_\|\varepsilon_c + \frac{\varepsilon_c\alpha}{2}\bar{\nabla}_\|\delta_\kappa + \varepsilon_c\left[\left(1+\frac{\delta_{0\kappa}}{2}\right)-\frac{\delta_\kappa}{2}\right]\bar{\nabla}_\|\alpha\right\}. \tag{A.1}$$

Using equations (18) and (19), and considering that $\varepsilon_c \gg 1$ we obtain that

$$\nabla_\|\varepsilon_c \approx \left(\frac{c}{c_{A0}}\right)^2\left\{T\bar{n}\nabla_\|\mathcal{B} + K\nabla_\|\bar{n}\right\}, \tag{A.2}$$

$$\nabla_\|\delta_\kappa = \beta_{\kappa 0}\left\{S\bar{n}\nabla_\|\mathcal{B} + P\nabla_\|\bar{n}\right\}, \tag{A.3}$$

where $T = -(2\mathcal{B}-\bar{\omega})/[\mathcal{B}^2(\mathcal{B}-\bar{\omega})^2]$ and $S = (3/2)\bar{\omega}/(\mathcal{B}-\bar{\omega})^4$. Using the previous relations in Equation (A.1) we obtain that

$$\bar{f}_{(s)\|} = (A_1+\beta_{\kappa 0}A_2)\,\bar{n}^{1/2} + \beta_{\kappa 0}A_3\bar{n}^{3/2} + (A_4+\beta_{\kappa 0}A_5)\,\bar{n}^{-1/2}\bar{\nabla}_\|\bar{n} + \beta_{\kappa 0}A_6\bar{n}^{1/2}\bar{\nabla}_\|\bar{n}, \tag{A.4}$$

where

$$A_1 = \frac{(1-\bar{\omega})^{1/2}}{4K^{1/2}}\left(-\frac{\alpha}{2}T\bar{\nabla}_\|\mathcal{B} + K\bar{\nabla}_\|\alpha\right), \tag{A.5}$$

$$A_2 = \frac{(1-\bar{\omega})^{1/2}}{4K^{1/2}}\left(-\frac{\alpha}{2}GT\bar{\nabla}_\|\mathcal{B} + KG\bar{\nabla}_\|\alpha\right), \tag{A.6}$$

$$A_3 = \frac{(1-\bar{\omega})^{1/2}}{4K^{1/2}}\left[\frac{\alpha}{2}(PT+KS)\,\bar{\nabla}_\|\mathcal{B} - \frac{KP}{2}\bar{\nabla}_\|\alpha\right], \tag{A.7}$$

$$A_4 = -\alpha\frac{(1-\bar{\omega})^{1/2}}{8}K^{1/2}, \tag{A.8}$$

$$A_5 = -\alpha\frac{(1-\bar{\omega})^{1/2}}{8}K^{1/2}G, \tag{A.9}$$

$$A_6 = \frac{3}{16}\alpha(1-\bar{\omega})^{1/2}PK^{1/2}, \tag{A.10}$$

where $G = -(1/4)\bar{\omega}/(1-\bar{\omega})^3$.

Appendix A.2: MMP term

Using (25) and (28) and neglecting terms at the second order of the plasma beta, we can deduce that the ponderomotive magnetic moment is given by

$$M = \frac{|E|^2}{16\pi B_0}\left(\frac{\partial\varepsilon_c}{\partial\mathcal{B}} - \varepsilon_c\frac{\partial\delta_\kappa}{\partial\mathcal{B}}\right). \tag{A.11}$$

The partial derivatives are given by

$$\frac{\partial\varepsilon_c}{\partial\mathcal{B}} = -\left(\frac{c}{c_{A0}}\right)^2\frac{(2\mathcal{B}-\bar{\omega})}{\mathcal{B}^2(\mathcal{B}-\bar{\omega})^2}\bar{n} = \left(\frac{c}{c_{A0}}\right)^2 T\bar{n}, \tag{A.12}$$

$$\frac{\partial\delta_\kappa}{\partial\mathcal{B}} = \frac{3}{2}\beta_{\kappa 0}\frac{\bar{\omega}}{(\mathcal{B}-\bar{\omega})^4}\bar{n} = \beta_{\kappa 0}S\bar{n}. \tag{A.13}$$

Therefore, we have that the magnetic moment pumping along the magnetic field lines $f_{(MMP)\|} = B_0R_pM\bar{\nabla}_\|\mathcal{B}$ is given by

$$f_{(MMP)\|} = (A_7+\beta_{\kappa 0}A_8)\,\bar{n}^{1/2} + \beta_{\kappa 0}A_9\bar{n}^{3/2}, \tag{A.14}$$

where,

$$A_7 = \frac{(1-\bar{\omega})^{1/2}}{4K^{1/2}}\alpha T\bar{\nabla}_\|\mathcal{B}, \tag{A.15}$$

$$A_8 = \frac{(1-\bar{\omega})^{1/2}}{4K^{1/2}}\alpha TG\bar{\nabla}_\|\mathcal{B}, \tag{A.16}$$

$$A_9 = \frac{(1-\bar{\omega})^{1/2}}{4K^{1/2}}\left(\frac{PT}{2} - KS\right)\alpha\bar{\nabla}_\|\mathcal{B}. \tag{A.17}$$

Appendix A.3: Terms in the ODE

We can calculate explicitly the terms Φ_i (we do it for $\alpha = 1$) involved in the ODE given by Equation (31),

$$\Phi_1(x_\|,\beta_{\kappa 0}) = -\frac{(1-\bar{\omega})^{1/2}}{8}\left(1-\beta_{\kappa 0}\frac{\bar{\omega}}{4(1-\bar{\omega})^3}\right) \times \frac{(2\mathcal{B}(x_\|)-\bar{\omega})}{\mathcal{B}(x_\|)^{3/2}(\mathcal{B}(x_\|)-\bar{\omega})^{3/2}}\bar{\nabla}_\|\mathcal{B}(x_\|), \tag{A.18}$$

$$\Phi_2(x_\|,\beta_{\kappa 0}) = \beta_{\kappa 0}\frac{\bar{\omega}(1-\bar{\omega})^{1/2}}{8}\frac{\left(\frac{1}{2}\mathcal{B}(x_\|)-\bar{\omega}\right)}{\mathcal{B}(x_\|)^{3/2}(\mathcal{B}(x_\|)-\bar{\omega})^{9/2}}\bar{\nabla}_\|\mathcal{B}(x_\|), \tag{A.19}$$

$$\Phi_3(x_\|,\beta_{\kappa 0}) = \frac{1}{8}\sqrt{\frac{1-\bar{\omega}}{\mathcal{B}(x_\|)(\mathcal{B}(x_\|)-\bar{\omega})}}\left(1-\beta_{\kappa 0}\frac{\bar{\omega}}{(1-\bar{\omega})^3}\right), \tag{A.20}$$

$$\Phi_4(x_\|,\beta_{\kappa 0}) = \beta_{\kappa 0}\frac{3}{32}\frac{(1-\bar{\omega})^{1/2}\bar{\omega}}{\mathcal{B}(x_\|)^{1/2}(\mathcal{B}(x_\|)-\bar{\omega})^{7/2}}. \tag{A.21}$$

Appendix B: Empirical estimation of magnetospheric plasma parameters

Appendix B.1: Earth

To obtain an estimated average equatorial plasma density profile n_{est} in Earth's magnetosphere, we use Carpenter & Anderson (1992) empirical model, derived from International Sun-Earth Explorer 1 (ISEE 1) satellite measurements and whistler data. The model is valid for the range $2.25 < L < 8$ and 00-15MLT under relatively steady global magnetic conditions. It is defined piecewise for the "saturated" plasmasphere ($2.25 \leq L \leq L_{\mathrm{ppi}}$), the plasmapause ($L_{\rm ppi} < L < L_{\rm ppo}$), and the plasma trough ($L_{\rm ppo} < L \leq 8$)

$$\frac{n_{\rm est}(L)}{\rm cm^{-3}} = \begin{cases} 10^{-(0.3145L-3.9043)} & ,2.25 \leq L \leq L_{\rm ppi} \\ n_0(L_{\rm ppi})10^{-\frac{(L-L_{\rm ppi})}{(0.1+0.011(t-6))}} & ,L_{\rm ppi} \leq L \leq L_{\rm ppo} \\ (5800+300t)\left(\frac{L}{L_{\rm ppo}}\right)^{-4.5} & \\ +\left(1-e^{-(L-2)/10}\right) & ,L_{\rm ppo} \leq L \leq 8 \end{cases} \tag{B.1}$$

For this analysis, we set $t = 12$ (noon) and $L_{\rm ppi} = 5$, consistent with typical plasmaspheric observations where $L_{\rm ppi}$ extends up to $\sim$ 4-5R_E. The outer boundary $L_{\rm ppo}$ of the plasmapause, a sharp density gradient region typically narrower than 0.5L (Kwon et al. 2015), is determined by demanding continuity

$$n_0(L_{\rm ppi})10^{-\frac{(L_{\rm ppo}-L_{\rm ppi})}{(0.1+0.011(t-6))}} = (5800+300t)+\left(1-e^{-(L_{\rm ppo}-2)/10}\right).$$

This profile is shown in Figure B.1.a.

For the estimated magnetic field magnitude $B_{\rm est}$, we consider Mead (1964) distorted dipole model, which accounts for the dayside compression of the geomagnetic field by solar wind pressure. The equatorial magnetic field magnitude (in nT) at noon is

$$\frac{B_{\rm est}(L)}{\rm nT} = \left(\frac{3.1}{L^3}+\frac{2.515}{r_b^3}+\frac{\sqrt{3}\times 1.215}{r_b^4}L\right)\times 10^4, \tag{B.2}$$

where $r_b = 10$ is the adopted typical normalized distance (in R_E) to the magnetopause (Cahill & Patel 1967). Because this model incorporates surface currents at the magnetopause boundary, the field decays more slowly than a pure dipolar field $B_{\rm dipolar} \sim (3.1/L^3)\times 10^4$nT, as compared in Figure B.1.b.

Using Equations B.1 and B.2, the estimated Alfvén velocity $c_{\rm A,est}$ applied in section 7 for the Earth's magnetosphere is

$$\frac{c_{\rm A,est}}{c} = \frac{B_{\rm est}}{\sqrt{4\pi M n_{\rm est}}} \sim \frac{(B_{\rm est}/\rm nT)}{\sqrt{(M/m_{\rm p})(n_{\rm est}/\rm cm^{-3})}}\times\left(7.27\times 10^{-5}\right) \tag{B.3}$$

where m_p is the proton mass and M the ion mass. Since protons mainly populate Earth's magnetosphere, we can consider $M = m_{\rm p}$. Based on these estimations $c_{\rm A,est}/c \sim 10^{-3}$ - 8×10^{-3} for all L-shell values considered ($2.25 \leq L \leq 8$), consistent with standard observations (Sarris et al. 2009).

To estimate average thermal pressure, we use proton distribution data from the Charge-Energy-Mass Spectrometer (CHEM) aboard the Charge Composition Explorer (CCE) satellite of the Active Magnetospheric Particle Tracer Explorers (AMPTE) mission, averaged over 1985-1987 (De Michelis et al. 1999). We extracted perpendicular and parallel proton pressures (in nPa) via WebPlotDigitizer (Rohatgi 2024) and fitted them to a gamma-type empirical function, $P(L)/\rm nPa = AL^a \exp^{-bL}$. The resulting best-fit parameters (A, b, a) are $(0.100, 7.466, 1.688)$ for the perpendicular component $P_{\perp,\rm est}$, and $(0.047, 7.431, 1.617)$ for the parallel component $P_{\parallel,\rm est}$. The total isotropic pressure $P_{\rm est} = \frac{1}{3}(P_{\parallel,\rm est}+2P_{\perp,\rm est})$ yields an average plasma beta of

$$\beta_{\rm est} = \frac{8\pi(P_{\rm est}/\rm nPa)}{(B_{\rm est}/\rm nT)^2}\times 10^2. \tag{B.4}$$

As shown in Figure B.1.c, $\beta_{\rm est} \sim 0.1$ near the magnetopause and drops below 10^{-3} inside the plasmasphere.

Appendix B.2: Jupiter

To obtain an estimated average equatorial plasma density profile in the inner Jovian magnetosphere, we consider the observations reported by Bagenal (1994). This study presents a description of the plasma conditions in the Io plasma torus, between $L = 5$ and $L = 10R_J$, based on Voyager 1 data collected in March 1979. In their analysis, the plasma characteristics observed along the spacecraft trajectory were extrapolated along magnetic field lines by numerically solving the diffusive equilibrium equations. This method yielded radial profiles of plasma properties at the centrifugal equator, as well as meridian-plane density maps for the major ionic species.

Using WebPlotDigitizer (Rohatgi 2024), we extracted the radial density profiles (in cm^{-3}) for each ionic species at the centrifugal equator as presented in that study. We then fit these profiles on a logarithmic scale using a combination of a Gaussian function (representing the torus source of newborn ions) and two additional functions that capture the slope of the density decrease as L increases. Thus, for each species α, the estimated density is given by $n_{\rm est,\alpha}(L) = f_{\rm core}(L) + [1-\sigma_1(L)]\sigma_2(L)f_{\rm ledge}(L) + [1-\sigma_2(L)]f_{\rm tail}(L)$, where

$$f_{\rm core}(L) = A_c e^{-(L-L_c)^2/2D_c^2},$$
$$f_{\rm ledge}(L) = A_1 10^{-b_1 L},$$
$$f_{\rm tail}(L) = A_2 10^{-b_2 L},$$
$$\sigma_1(L) = \left(1+e^{2(L-L_1)/D_1}\right)^{-1},$$
$$\sigma_2(L) = \left(1+e^{2(L-L_2)/D_2}\right)^{-1}.$$

The best-fit values for each species are listed in Table B.1, and the corresponding estimated average density profiles are shown in Figure B.2.a. In this cold region of the inner torus, the composition is dominated by S^+ and O^+ ions, with significant contributions from S^{++}, S^{+++}, and O^{++}. Furthermore, an upper limit of 0.5% can be placed on the proton density in the cold torus (Bagenal 1994), based on the portion of the distribution extending above 10 eV. This makes protons a minor constituent of the ion plasma in this inner region. However, in the middle magnetosphere, protons comprise a significant fraction (20–50%) of the total plasma (McNutt Jr. et al. 1981).

We compare the total density predicted by our estimation (Figure B.2.a, black solid line) with the empirical model by Bagenal & Delamere (2011), which combines Voyager and Galileo plasma sheet measurements from the outer boundary of Io's orbit ($L \sim 6$) to $L \sim 50$

$$\frac{n_{\rm est}(L)}{\rm cm^{-3}} = 1987\left(\frac{L}{6}\right)^{-8.2} + 14\left(\frac{L}{6}\right)^{-3.2} + 0.05\left(\frac{L}{6}\right)^{-0.65}. \tag{B.5}$$

This model is depicted by the dotted black line in Figure B.2.a. The two profiles are highly consistent.

For the magnetic field magnitude, we assume a standard dipole model

$$B_{\rm est}(L) = \frac{4.17\times 10^5}{L^3}\,\rm nT. \tag{B.6}$$

This approximation remains valid in the inner Jovian magnetosphere up to $L \sim 10$, where contributions from currents flowing in the magnetospheric equatorial plasma sheet (the magnetodisc) are negligible (Connerney et al. 1981; Khurana et al. 2004). The corresponding profile is shown in Figure B.2.b.

Because our framework assumes a single-ion species, we must self-consistently adapt our equations to this multi-species environment to account for the different mass populations. We achieve this by defining an effective ion mass $M_{\rm eff}$ and an effective charge $q_{\rm eff}$ as follows

$$M_{\rm eff} = \frac{1}{n_{\rm est,Total}} \sum_{\alpha} n_{{\rm est},\alpha} m_{\alpha}, \tag{B.7}$$

$$q_{\rm eff} = \frac{1}{n_{\rm est,Total}} \sum_{\alpha} n_{{\rm est},\alpha} q_{\alpha}, \tag{B.8}$$

where $n_{\rm est,Total} = \sum_{\alpha} n_{{\rm est},\alpha}$. Averaging these quantities over the considered L-shell range (denoted by $\langle\rangle$) yields an average effective mass $\langle M_{\rm eff}\rangle$ and charge $\langle q_{\rm eff}\rangle$. By substituting $M = \langle M_{\rm eff}\rangle \sim 21.831\, m_p$ into Equation B.3, we estimate the Alfvén velocity for the Jovian magnetosphere. Based on these calculations, we obtain $c_{A,{\rm est}}/c \sim 7\times10^{-4} - 2\times10^{-3}$ across the evaluated range ($5 \le L \le 10$).

Consequently, the ion gyrofrequency Ω_0 used to normalize the wave frequency is no longer the proton gyrofrequency Ω_{H^+} (as is the case on Earth). Instead, it must be adjusted to $\Omega_0 \sim \left[(\langle q_{\rm eff}\rangle/e)\,/\left(\langle M_{\rm eff}\rangle/m_p\right)\right]\Omega_{H^+} \sim 6.40\times10^{-2}\Omega_{H^+}$, given that $\langle q_{\rm eff}\rangle \sim 1.397\, e$, with e representing the elementary charge.

Finally, to estimate the average plasma beta, we rely on bulk plasma parameters derived from Voyager 1 and 2 data (Mauk et al. 1996), covering the vicinity of the Io plasma torus, the inner magnetosphere, and a portion of the middle magnetosphere ($5 \le L \le 20$). We extracted these plasma beta values using WebPlotDigitizer (Rohatgi 2024) and fitted them to a double-sigmoid empirical function

$$\log_{10}(\beta_{\rm est}(L)) = C + \frac{A_1}{1+e^{-k_1(L-x_1)}} + \frac{A_2}{1+e^{-k_2(L-x_2)}}. \tag{B.9}$$

The resulting best-fit parameters $(C, A_1, k_1, x_1, A_2, k_2, x_2)$ are $(-2.979, 1.696, 5.633, 7.242, 1.262, 2.748, 9.593)$.

Appendix B.3: Saturn

To estimate the average equatorial plasma density profile in Saturn's inner magnetosphere, we rely on electron and ion density measurements from the Radio and Plasma Wave Science (RPWS) and Cassini Plasma Spectrometer (CAPS) instruments on board the Cassini spacecraft, collected between June 2004 and September 2007 Persoon et al. (2009). The observations cover latitudes from the equator to 35° and radial distances $3.6 \le L \le 10$. This inner region is heavily populated by water-group ions (W^+) originating from the plumes of Enceladus' southern polar region, alongside hydrogen ions (H^+).

At lower L values, ion densities increase radially toward a broad equatorial peak, remaining approximately constant in the $4 < L \le 5$ range. The equatorial density profile for W^+ reaches a maximum of $62\,{\rm cm}^{-3}$ at $L = 4.8$, while H^+ peaks at $9\,{\rm cm}^{-3}$ at $L = 4.6$. Beyond $L = 5$, both species diffuse radially outward, exhibiting inverse L-shell dependencies: $n_{{\rm eq},W^+} \propto L^{-4.3}$ and $n_{{\rm eq},H^+} \propto L^{-3.2}$.

Using these observations, we approximate the total estimated number density $n_{\rm est,Total}$ for $4 < L \le 10$ by assuming a constant peak density up to $L = 5$ and subsequently applying the respective decay rates:

$$\frac{n_{\rm est,Total}(L)}{{\rm cm}^{-3}} = \begin{cases} 59 & 4 < L \le 5 \\ n_{{\rm est},W^+}(L) + n_{{\rm est},H^+}(L) & 5 < L \le 10 \end{cases} \tag{B.10}$$

where $n_{{\rm est},W^+}(L) = 52(L/5)^{-4.3}$ and $n_{{\rm est},H^+}(L) = 7\,(L/5)^{-3.2}$ are the estimated density profiles for water-group ions and protons, respectively. While more comprehensive models are necessary for extended radial distances (Bagenal & Delamere 2011), this piecewise function sufficiently captures the density profile required for our analysis in the inner magnetosphere.

As shown in Figure B.3.a, Saturn's inner magnetosphere is strongly dominated by heavy water-group ions (W^+). To self-consistently adapt our single-ion equations to this multi-species environment, we define an average effective ion mass $M_{\rm eff} = \langle (m_p n_{{\rm est},H^+} + 18 m_p n_{{\rm est},W^+})/n_{\rm est,Total}\rangle \sim 15.262\, m_p$ and an effective charge $q_{\rm eff} = 1$. Consequently, the adjusted equatorial ion gyrofrequency becomes $\Omega_{i0} \sim 6.55\times10^{-2}\,\Omega_{H^+}$.

Finally, to estimate the magnetic field magnitude and average plasma beta, we rely on the study by Sergis et al. (2017), which analyzes particle and magnetic field data collected between July 2004 and December 2013 by the Cassini spacecraft in Saturn's equatorial magnetosphere, covering radial distances from 5 to $16R_S$.

They provide empirical polynomial fits for the dayside pressure (in Pa) and the magnetic field z-component (in nT). Although these fits are officially valid for $5 < L < 16$, we extend their application inward up to $L = 4$:

$$\log_{10} P_{\rm est}(L) = a_0 + a_1 L + a_2 L^2 + a_3 L^3 + a_4 L^4, \tag{B.11}$$

$$\log_{10} B_{z,{\rm est}}(L) = d_0 + d_1 L + d_2 L^2 + d_3 L^3, \tag{B.12}$$

where $(a_0, a_1, a_2, a_3, a_4) = (-17.96, 3.73, -0.5697, 0.0353$ $-0.0007795)$ and $(d_0, d_1, d_2, d_3) = (4.338, -0.5568, 0.0286, -0.0005052)$. The fitted component B_z corresponds to the off-equator (north-south) magnetic field. However, because their analysis was restricted to measurements where $|B_r| < 0.5\,$nT and $|B_r| < 0.2|B|$, we can safely assume $B_{\rm est} \sim B_{z,{\rm est}}$. As illustrated in Figure B.3.b, this field decays faster than a pure dipolar field, $B_{\rm dipolar} \sim (2.1\times10^4/L^3)\,$nT. This accelerated decay is driven by the centrifugal expansion of the trapped plasma, which forms a magnetodisc and drives an equatorial ring current whose induced magnetic field opposes the planetary dipole in the inner and middle magnetosphere (Connerney et al. 1983; Arridge et al. 2008). Based on these estimations, we obtain $c_{A,{\rm est}}/c \sim 1\times10^{-4} - 8\times10^{-4}$ across the evaluated range ($3.6 \le L \le 10$).

Figure B.3.c presents the estimated equatorial plasma beta profile as a function of L. The plasma beta increases with radial distance, remaining > 1 beyond $L \sim 8$–$10R_S$ across all local times (Sergis et al. 2017), and reaches peak values of $\beta \sim 3$, 4, and 6–8 for the dayside, dawn, and dusk/nightside sectors, respectively. Conversely, moving toward the inner magnetosphere, the magnetic field strength increases sharply with decreasing radial distance. This causes the plasma beta to drop rapidly, becoming < 0.1 at $L = 5R_S$ for all local times. On the dayside, $\beta < 0.3$ for $L < 7$. Since our theoretical framework requires a low-beta regime, this restricted interval is the primary focus of our analysis.

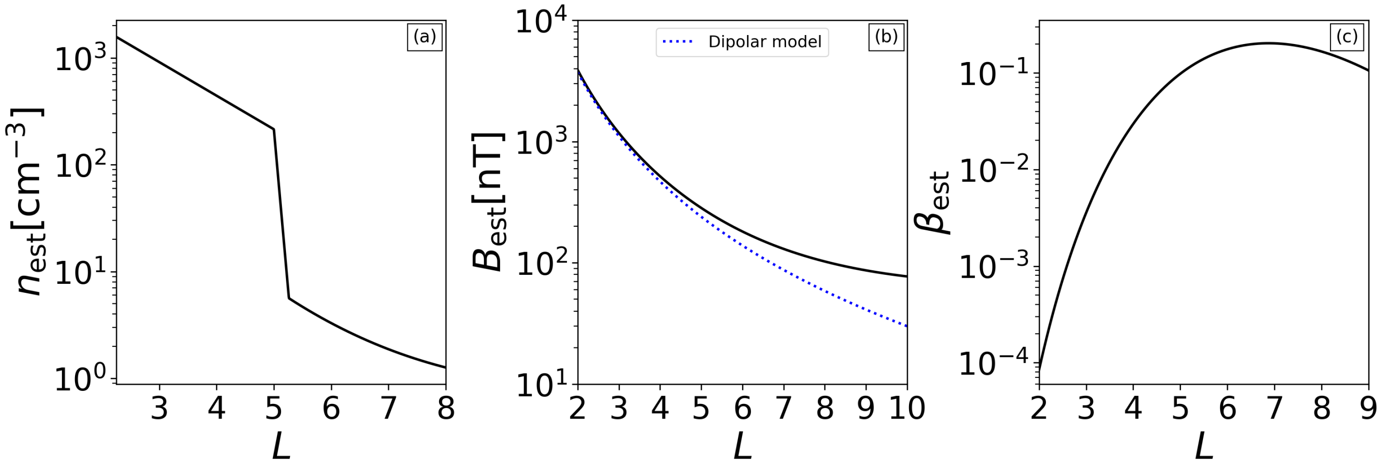

Fig. B.1. Empirical estimates of the average equatorial plasma parameters in Earth's dayside magnetosphere as a function of L-shell. Panel (a): Estimated plasma density, n_{est} (cm^{-3}).Panel (b): Estimated magnetic field magnitude, B_{est} (black solid line, nT), compared to the standard terrestrial dipole model (blue dotted line).Panel (c): Estimated plasma beta, β_{est}.

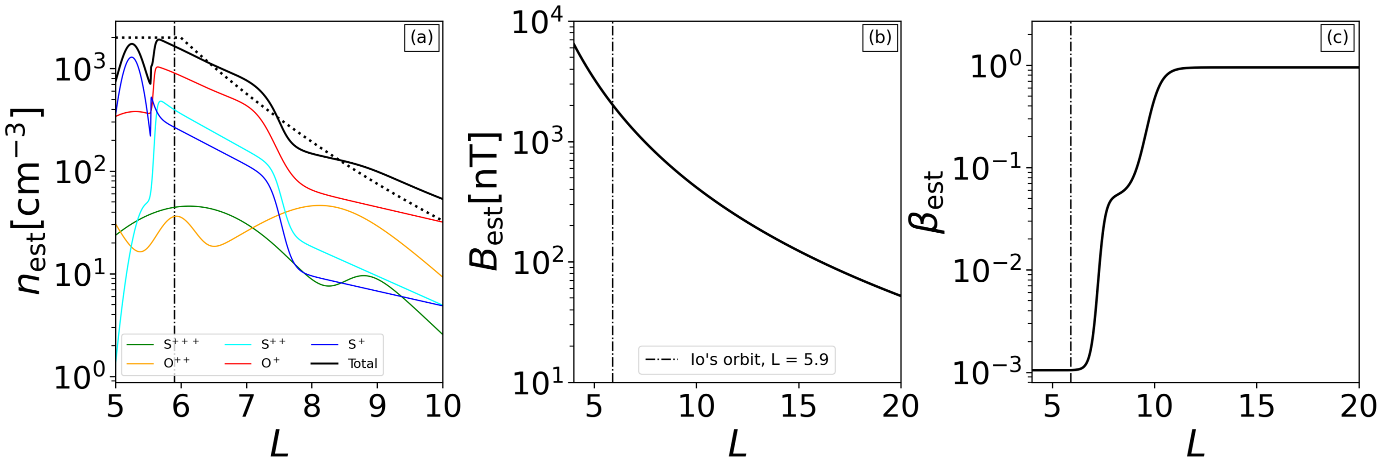

Fig. B.2. Empirical estimates of the average equatorial plasma parameters in Jupiter's dayside magnetosphere as a function of L-shell. Panel (a) Estimated plasma density, $n_{est,\alpha}$ (cm^{-3}) for each species α. Solid lines denote the major ion species: O^+ (red), O^{++} (orange), S^+ (blue), S^{++} (cyan), S^{+++} (green), and the total density (black). The empirical density model by Bagenal & Delamere (2011) is shown as a dotted black line. Panel (b): Estimated magnetic field magnitude, B_{est} (nT). Panel (c): Estimated plasma beta, β_{est}. Across all panels, the dash-dotted black line indicates Io's orbit at $L = 5.9$.

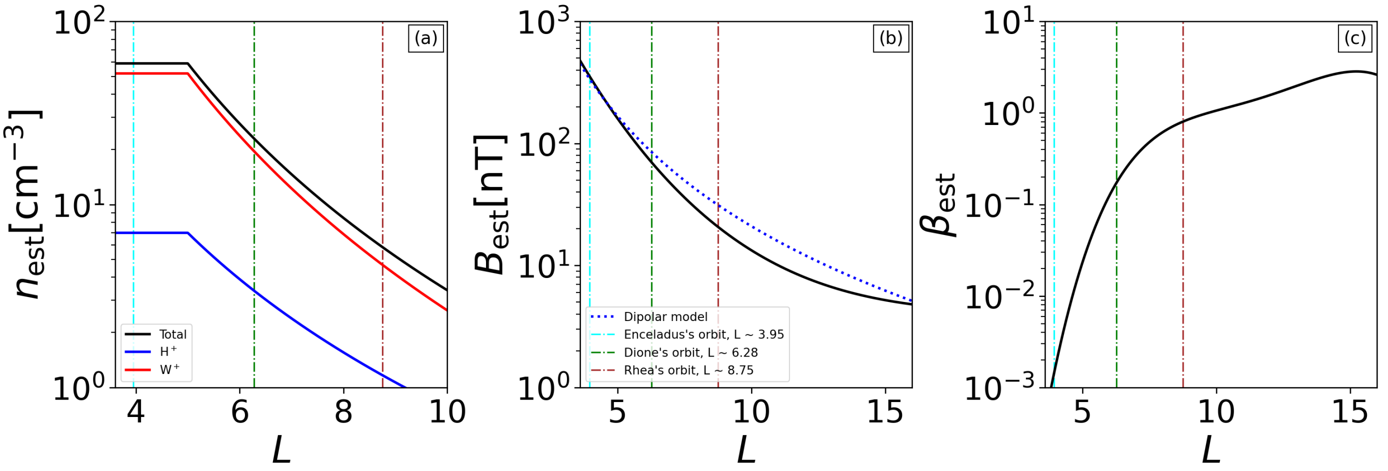

Fig. B.3. Empirical estimates of the average equatorial plasma parameters in Saturn's dayside magnetosphere as a function of L-shell. Panel (a): Estimated plasma density, $n_{\text{est},\alpha}$ (cm^{-3}) for each species α. Solid lines denote the specific ion species: W^+ (red), H^+ (blue), and total density (black). Panel (b) Estimated magnetic field magnitude, B_{est} (black solid line, nT), compared to the standard Saturnian dipole model (blue dotted line). Panel (c) Estimated plasma beta, β_{est}. Across all panels, dash-dotted lines mark the orbits of the main moons: Enceladus (cyan, $L \sim 3.95$), Dione (green, $L \sim 6.28$), and Rhea (brown, $L \sim 8.75$).

Table B.1. Best-fit values for the estimated density profile in the Jovian magnetosphere for each species.

Species	A_c	L_c	D_c	L_1	D_1	L_2	D_2	A_1	b_1	A_2	b_2
O^+	3.810 (2)	5.306	6.453 (-1)	5.586	2.626 (-2)	7.325	2.947 (-1)	4.330 (3)	1.389 (-1)	9.437 (2)	1.471 (-1)
S^+	1.290 (3)	5.248	1.520 (-1)	5.541	2.949 (-3)	7.462	1.718 (-1)	2.429 (4)	3.319 (-1)	1.341 (2)	1.440 (-1)
S^{++}	4.817 (1)	5.497	1.841 (-1)	5.614	4.266 (-2)	7.500	1.440 (-1)	4.799 (4)	3.538 (-1)	3.467 (3)	2.846 (-1)
O^{++}	2.523 (1)	5.922	2.492 (-1)	1.139 (-3)	2.253 (-3)	8.247	8.831 (-1)	1.384 (8)	1.342	4.001 (6)	5.626 (-1)
S^{+++}	4.561 (1)	6.125	9.810 (-1)	-	-	8.676	4.185 (-1)	0	-	2.200 (6)	5.936 (-1)

Notes. The numbers in parentheses represent the magnitude order.